





# Covariant density functional theory input for $r$ -process simulations in actinides and superheavy nuclei: The ground state and fission properties

A. Taninah <sup>1</sup>, S. E. Agbemava <sup>1,2</sup> and A. V. Afanasjev <sup>1</sup>

<sup>1</sup>*Department of Physics and Astronomy, Mississippi State University, Mississippi State, Mississippi 39762, USA*

<sup>2</sup>*Ghana Atomic Energy Commission, National Nuclear Research Institute, P.O. Box LG80, Legon, Ghana*

 (Received 25 May 2020; revised 20 September 2020; accepted 26 October 2020; published 30 November 2020)

A systematic investigation of the ground-state and fission properties of even-even actinides and superheavy nuclei with  $Z = 90$ – $120$  from the two-proton up to two-neutron drip lines with proper assessment of systematic theoretical uncertainties has been performed for the first time in the framework of covariant density functional theory (CDFT). These results provide a necessary theoretical input for the  $r$ -process modeling in heavy nuclei and, in particular, for the study of fission cycling. Four state-of-the-art globally tested covariant energy density functionals (CEDFs), namely, DD-PC1, DD-ME2, NL3\*, and PC-PK1, representing the major classes of the CDFT models are employed in the present paper. Ground-state deformations, binding energies, two-neutron separation energies,  $\alpha$ -decay  $Q_\alpha$  values and half-lives, and the heights of fission barriers have been calculated for all these nuclei. Theoretical uncertainties in these physical observables and their evolution as a function of proton and neutron numbers have been quantified and their major sources have been identified. Spherical shell closures at  $Z = 120$ ,  $N = 184$ , and  $N = 258$  and the structure of the single-particle (especially, high- $j$ ) states in their vicinities as well as nuclear matter properties of employed CEDFs are two major factors contributing to theoretical uncertainties. However, different physical observables are affected in a different way by these two factors. For example, theoretical uncertainties in calculated ground-state deformations are affected mostly by the former factor, while theoretical uncertainties in fission barriers depend on both of these factors.

DOI: [10.1103/PhysRevC.102.054330](https://doi.org/10.1103/PhysRevC.102.054330)

## I. INTRODUCTION

The majority of the nuclei found in nature are formed in the astrophysical rapid neutron-capture process ( $r$  process). Indeed, the  $r$  process is responsible for the synthesis of approximately half of the nuclei in nature beyond Fe [1] and it is the only process which leads to the creation of nuclei heavier than Bi [2]. It takes place at extremely high neutron densities ( $N_n \geq 10^{20} \text{ cm}^{-3}$ ) which are high enough to make neutron capture faster than  $\beta$  decay even for the nuclei with neutron excess between 15 to 30 units from the stability line. The production of neutron-rich nuclei located in the vicinity of the neutron drip line is enabled under these conditions via neutron capture and ( $\gamma, n$ ) photodisintegration during the  $r$  process. Once the neutron source ceases, the progenitor nuclei decay either via  $\beta^-$  decay or  $\alpha$  emission or by fission processes (such as neutron-induced,  $\beta$ -delayed, and spontaneous fissions) towards stability and form the stable isotopes of elements up to the heaviest species Th, U, and Pu. The typical timescale of the  $r$  process is in the seconds range [2–4].

Over the years different possible astrophysical sites have been and still are considered as possible candidates for the  $r$  process. These include core-collapse supernovas, magnetorotational core-collapse supernovas, accretion disk outflows from collapsars, neutron star (NS) mergers and neutron star–black hole mergers, etc. [2–5]. So far only the NS merger is experimentally confirmed as a site of the  $r$  process via the

observation of gravitational waves from the GW170817 neutron star merger [6] with simultaneous observation of the AT 2017gfo macronova/kilonova afterglow [7]. In NS mergers, the  $r$ -process material originates in the NS crust, and the composition of the crust and how it responds to stress caused by the merger dictate the amount of the  $r$ -process material which is ejected. The NS merger produces approximately  $10^{-2} M_\odot$  of ejected  $r$ -process matter in the dynamic ejecta and a similar amount in the accretion disk outflows [4,8,9]. Although some uncertainties still exist, at present the NS merger is considered as the major astrophysical site of the  $r$  process providing the dominant source of heavy nuclei [2,4,5].

The modeling of the  $r$  process in such neutron-rich environments depends sensitively on nuclear masses,  $\alpha$ - and  $\beta$ -decay half-lives, neutron capture, and fission properties of the nuclei, the majority of which will never be measured in laboratory conditions [2,4,5,10]. Nuclear masses determine the flow path of the  $r$  process,  $\beta$ -decay rates are responsible for the speed with which the  $r$  process moves matter to heavier nuclei,  $\alpha$  decays become important in heavy nuclei as competing decay channels, and neutron captures drive the nuclei towards the neutron-rich side of the nuclear landscape. Of special interest in the context of the present paper are fission properties. Fission needs to be considered in the  $r$ -process simulations if the neutron-to-seed ratio is large enough to produce fissioning nuclei [11–14]. If the initial neutron-to-seed ratio is large ( $\geq 100$ ) the  $r$  process can reach the region near

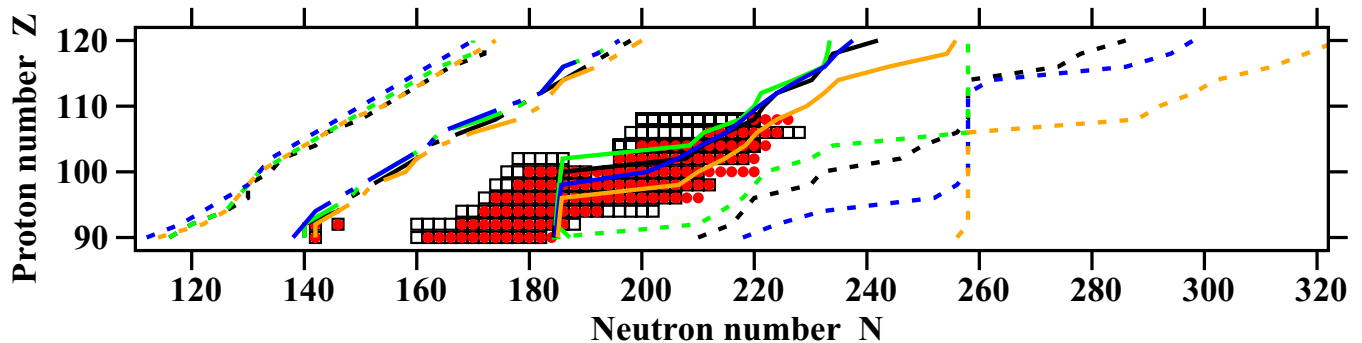


FIG. 1. The part of the nuclear chart under study. Black, green, blue, and orange lines are used for the results obtained with the DD-PC1, DD-ME2, NL3\*, and PC-PK1 CEDFs, respectively. Two-proton and two-neutron drip lines predicted by four CEDFs are shown by dashed lines. Two samples of the distribution of the abundances of heavy and superheavy elements in the  $r$ -process simulations are shown by open squares (based on the bottom panel of Fig. 8 of Ref. [15]) and red circles (based on Fig. 3 of Ref. [16]). The former results correspond to hot  $r$ -process conditions and are based on the ETFS/ETFSI combination of fission barriers and mass predictions (see Ref. [15]). The latter results have been obtained in Ref. [16] based on fission properties obtained with the BCPM energy density functional. Note that these  $r$ -process calculations are restricted to the  $Z \leq 110$  nuclei. The  $r$ -process path is shown here approximately by solid lines corresponding to two-neutron separation energy  $S_{2n} = 4.0$  MeV. The  $r$ -process proceeds along the lines of constant neutron separation energies towards heavy nuclei that for typical conditions during the  $r$ -process correspond to  $S_n^0$  approximately located between 2 and 3 MeV [1,17]. However, due to neutron pairing being stronger at even neutron numbers  $N$  the most abundant isotopes always have even  $N$  values. For this reason, we follow Refs. [1,17] and characterize the  $r$ -process path [the path in the  $(Z, N)$  plane corresponding to an isotope with highest abundance in each isotopic chain] as the path which satisfies the condition that two-neutron separation energy  $S_{2n}$  has the value  $S_{2n} = 2S_n^0$ . Dot-dashed lines show the beta-stability lines for four functionals.

and beyond neutron shell closure at  $N = 184$ , where fission plays a dominant role (the examples of the distribution of abundances of actinides and superheavy elements as obtained in a pair of the  $r$ -process simulations are shown in Fig. 1). This is exactly the case for the NS mergers [12]. In this case, all fission channels (neutron induced, beta delayed, neutrino induced, and spontaneous fissions) need to be considered. Fission leads to the termination of the hot  $r$  process by means of fission cycling which returns matter to lighter nuclei [10]. It also determines the strength of fission cycling, the ratio of the actinides to light and medium mass  $r$ -process nuclei, and thus the shape of the final element abundance pattern. In addition, it defines the possibility of the formation of neutron-rich superheavy nuclei in the  $r$  process [15].

Thus, in the situation when experimental data are not known the outcome of the  $r$ -process modeling sensitively depends on the quality of employed theoretical frameworks and associated theoretical uncertainties and their propagation on going to neutron-rich nuclei. By tradition, the output of different theoretical frameworks is used for different physical observables (such as masses, the rates and half-lives of different decay channels and reactions, etc.) in the  $r$ -process modeling. Existing  $r$ -process calculations, which include information on fission properties, are based on the fission barrier heights obtained in nonrelativistic models [10,14,18]. So far fission barrier heights obtained in the finite range droplet model (FRDM), Thomas-Fermi (TF) model and extended Thomas-Fermi model with Strutinsky integral approach (ETFSI-Q), Hartree-Fock-Bogoliubov (HFB) model with Skyrme HFB-14 energy density functional (EDF), and BCPM EDF have been used in these calculations. Moreover the sets of fission barriers relevant for the  $r$ -process simulations have been generated in the FRDM in Ref. [18], in the

ETFSI-Q approach with the SkSC4 functional in Ref. [19], in the HFB models with Skyrme HFB-14, SV-min, SLy6, SkI3, SV-bas EDFs [20–22], Gogny D1M\* [23], and BCPM [18] functionals. Note that all these calculations assume axial symmetry of the nuclei.

Covariant density functional theory (CDFT) [24] is an alternative approach to the above-mentioned nonrelativistic methods and so far it has not been applied for a systematic study of fission properties of the nuclei relevant for the  $r$ -process modeling. However, this theory has a number of advantages over nonrelativistic methods which are discussed below. Covariant energy density functionals (CEDFs) exploit basic properties of QCD at low energies, in particular symmetries and the separation of scales [25]. They provide a consistent treatment of the spin degrees of freedom and spin-orbit splittings ([26,27]); the latter has an essential influence on the underlying shell structure. In addition, these functionals include *nuclear magnetism* [28], i.e., a consistent description of currents and time-odd mean fields important for odd-mass nuclei [29], the excitations with unsaturated spins, magnetic moments [30], and nuclear rotations [31,32]. Because of Lorentz invariance no new adjustable parameters are required for the time-odd parts of the mean fields [29]. This is contrary to the case of nonrelativistic Skyrme DFTs in which several prescriptions for fixing time-odd mean fields exist [33,34].<sup>1</sup> This fact could be extremely important in the applications to fission processes including dynamical correlations since

<sup>1</sup>Unfortunately, the role of time-odd mean fields in Gogny DFTs has not been studied so far and it is unknown whether they are uniquely defined.

time-odd mean fields have a significant impact on collective masses [35,36].

The goal of this paper is to close this gap in our knowledge and to perform the first systematic investigation within the CDFT framework of the ground-state and fission properties of the nuclei with proton numbers  $Z = 90$ –120 located between two-proton and two-neutron drip lines (see Fig. 1). This paper will not only provide an input for the  $r$ -process modeling but also evaluate the extension of the nuclear landscape up to the two-neutron drip line as well as estimate relevant theoretical uncertainties and their sources in the description of physical observables of interest. In addition, it will allow one for the first time to compare the predictions for fission barriers in the nuclei relevant for  $r$ -process modeling obtained in relativistic and nonrelativistic frameworks.

Considering the region of the nuclear chart in which the  $r$  process is expected to take place and the fact that there are no experimental data to benchmark theoretical results, it is important to estimate theoretical uncertainties in the predictions of physical observables of interest [37–39]. Theoretical uncertainties emerge from the underlying theoretical approximations. In the DFT framework, there are two major sources of these approximations, namely, the range of interaction and the form of the density dependence of the effective interaction [40,41]. In the nonrelativistic case one has zero range Skyrme and finite range Gogny forces and different density dependencies [40]. A similar situation exists also in the relativistic case: point coupling and meson exchange models have an interaction of zero and of finite range, respectively [24,42–44]. The density dependence is introduced either through an explicit dependence of the coupling constants [42,44,45] or via nonlinear meson couplings [41,43]. This ambiguity in the definition of the range of the interaction and its density dependence leads to several major classes of the covariant energy density functionals which were discussed in Ref. [39].

Since statistical uncertainties in the physical observables are smaller than systematic ones (see Ref. [46]), we focus here on the latter ones. They are related to the choice of EDF. We follow our previous publications on this topic [39,47–49] and define systematic theoretical uncertainty for a given physical observable (which we call in the following “spreads”) via the spread of theoretical predictions as [39]

$$\Delta O(Z, N) = |O_{\max}(Z, N) - O_{\min}(Z, N)|, \quad (1)$$

where  $O_{\max}(Z, N)$  and  $O_{\min}(Z, N)$  are the largest and smallest values of the physical observable  $O(Z, N)$  obtained within the set of CEDFs under investigation for the  $(Z, N)$  nucleus. Note that these spreads are only a crude approximation to the *systematic* theoretical errors discussed in Ref. [38] since they are obtained with a very small number of functionals which do not form an independent statistical ensemble. Note also that these *systematic* errors are not well defined in unknown regions of the nuclear chart or deformation since systematic biases of theoretical models could not be established in these regions in the absence of experimental data and/or an exact theory.

In order to consider several possible scenarios in the evolution of physical observables as a function of proton and neutron numbers and to evaluate systematic theoretical un-

certainties, the CEDFs NL3\* [43], DD-ME2 [42], DD-PC1 [44], and PC-PK1 [50] are used here<sup>2</sup> for all  $Z = 90$ –120 even-even nuclei located between two-proton and two-neutron drip lines.<sup>3</sup> These are state-of-the-art functionals representing the major classes of CDFTs (for more details see the discussion in Sec. II of Ref. [39] and the introduction to Ref. [59]). Their performance and related theoretical uncertainties have recently been analyzed globally in Refs. [39,48,49,68] and in particular in superheavy nuclei in Refs. [47,59]. They are characterized by an improved accuracy of the description of experimental data as compared with the previous generation of CEDFs. The fact that the NL3\*, DD-PC1, and PC-PK1 functionals reproduce empirical data on fission barrier heights in actinides [62–64,69] is especially important in the context of the present paper.

The paper is organized as follows. The theoretical framework and the details related to the calculations of the ground states and fission barriers are discussed in Sec. II. Section III is devoted to the analysis of the results of the calculations for ground-state properties. Theoretical results for  $\alpha$ -decay properties and related theoretical uncertainties are presented in Sec. IV. The heights of primary fission barriers (PFBs), their distribution in the  $(Z, N)$  plane, related theoretical uncertainties, and the comparison with nonrelativistic results are considered in Sec. V. Finally, Sec. VI summarizes the results of our paper.

<sup>2</sup>The compilation of Ref. [51] published in 2014 indicates the existence of 263 CEDFs ranging from simplest ansatz nonlinear meson exchange functionals such as NL1 [52] and NL3\* [43] to more microscopically motivated CEDFs such as G1, G2 [53], and DD-ME $\delta$  [54]. In addition, a number of new functionals were fitted in the time period between 2014 and 2020 (see, for example, Refs. [46,55–58]) so at present the total number of available CEDFs is likely to be in the vicinity of 300. Because of the extremely time-consuming nature of numerical calculations in this project, we use only the indicated last generation functionals. They outperform previous generation functionals in terms of the accuracy of global description of ground-state observables such as binding energies and charge radii [39,49,59,60], properly describe the regions of octupole deformation [48,61], and are able to reproduce experimentally known fission barriers in actinides [62–64].

<sup>3</sup>The present paper partially builds on previous results obtained by us. These are ground-state properties of the  $Z = 90$ –104 nuclei located between two-proton and two-neutron drip lines obtained in reflection symmetric RHB calculations with the NL3\*, DD-ME2, and DD-PC1 CEDFs in Ref. [39]; ground-state properties of octupole deformed nuclei with  $N < 210$  obtained in reflection asymmetric RHB calculations with NL3\*, DD-ME2, DD-PC1, and PC-PK1 functionals in Refs. [48,61]; and ground-state properties and the heights of inner fission barriers of superheavy nuclei with  $Z = 100$ –120,  $N \leq 196$  obtained in reflection symmetric RHB calculations with NL3\*, DD-ME2, DD-PC1, and PC-PK1 functionals in Refs. [47,59]. Additional information on the extension of the nuclear landscape to  $Z > 120$  obtained with DD-PC1 CEDF can be found in Refs. [65–67].

## II. THEORETICAL FRAMEWORK

In the present paper, the RHB framework with finite range pairing and its separable limit are used for a systematic study of ground-state properties of all even-even actinides ( $Z = 90\text{--}102$ ) and superheavy ( $Z = 104\text{--}120$ ) nuclei from the proton to neutron drip line. It has the proper coupling to the continuum at the neutron drip line and, therefore, it allows a correct description of weakly bound nuclei close to the neutron drip line.

The RHB equations for the fermions are given by [70]

$$\begin{pmatrix} \hat{h}_D - \lambda & \hat{\Delta} \\ -\hat{\Delta}^* & -\hat{h}_D + \lambda \end{pmatrix} \begin{pmatrix} U(\mathbf{r}) \\ V(\mathbf{r}) \end{pmatrix}_k = E_k \begin{pmatrix} U(\mathbf{r}) \\ V(\mathbf{r}) \end{pmatrix}_k. \quad (2)$$

Here,  $\hat{h}_D$  is the Dirac Hamiltonian for the nucleons with mass  $m$ ;  $\lambda$  is the chemical potential defined by the constraints on the average particle number for protons and neutrons;  $U_k(\mathbf{r})$  and  $V_k(\mathbf{r})$  are quasiparticle Dirac spinors [70–72]; and  $E_k$  denotes the quasiparticle energies. The Dirac Hamiltonian

$$\hat{h}_D = \boldsymbol{\alpha}(\mathbf{p} - \mathbf{V}) + V_0 + \beta(m + S) \quad (3)$$

contains an attractive scalar potential

$$S(\mathbf{r}) = g_\sigma \sigma(\mathbf{r}), \quad (4)$$

a repulsive vector potential

$$V_0(\mathbf{r}) = g_\omega \omega_0(\mathbf{r}) + g_\rho \tau_3 \rho_0(\mathbf{r}) + eA_0(\mathbf{r}), \quad (5)$$

and a magnetic potential

$$\mathbf{V}(\mathbf{r}) = g_\omega \boldsymbol{\omega}(\mathbf{r}) + g_\rho \tau_3 \boldsymbol{\rho}(\mathbf{r}) + e\mathbf{A}(\mathbf{r}). \quad (6)$$

The last term breaks time-reversal symmetry and induces currents. For example, time-reversal symmetry is broken when the time-reversed orbitals are not occupied pairwise; this takes place in odd-mass nuclei [29]. However, nuclear magnetism [28], i.e., currents and time-odd mean fields, plays no role in the studies of ground states and fission barriers in even-even nuclei. Thus, magnetic potential is neglected in the present RHB calculations.

In order to avoid the uncertainties connected with the definition of the size of the pairing window [73], we use the separable form of the finite range Gogny pairing interaction introduced by Tian *et al.* [74]. Its matrix elements in  $r$  space have the form

$$\begin{aligned} V(\mathbf{r}_1, \mathbf{r}_2, \mathbf{r}'_1, \mathbf{r}'_2) \\ = -G\delta(\mathbf{R} - \mathbf{R}')P(r)P(r')\frac{1}{2}(1 - P^\sigma) \end{aligned} \quad (7)$$

with  $\mathbf{R} = (\mathbf{r}_1 + \mathbf{r}_2)/2$  and  $\mathbf{r} = \mathbf{r}_1 - \mathbf{r}_2$  being the center of mass and relative coordinates. The form factor  $P(r)$  is of Gaussian shape:

$$P(r) = \frac{1}{(4\pi a^2)^{3/2}} e^{-r^2/4a^2}. \quad (8)$$

The two parameters  $G = 728 \text{ MeV fm}^3$  and  $a = 0.644 \text{ fm}$  of this interaction are the same for protons and neutrons and have been derived in Ref. [74] by a mapping of the  $^1S_0$  pairing gap of infinite nuclear matter to that of the Gogny force D1S [75]. This pairing provides a reasonable description of pairing properties in the actinides (see Refs. [39,76,77])

and has been used in our previous studies of different phenomena in actinides and in super- and hyperheavy nuclei in Refs. [39,48,59,61,65,66].

The truncation of the basis is performed in such a way that all states belonging to the major shells up to  $N_F = 20$  fermionic shells for the Dirac spinors and up to  $N_B = 20$  bosonic shells for the meson fields are taken into account. Note that the latter applies only to the NL3\* and DD-ME2 functionals which contain meson exchange. As follows from the investigation of Refs. [39,78] this truncation of basis provides sufficient numerical accuracy.

The calculations are performed in the following way.

- (1) Reflection-symmetric constrained axial RHB calculations (RS-RHB) are performed for each nucleus and the potential-energy curve is defined in a large deformation range from  $\beta_2 = -1.0$  to  $1.6$  in steps of  $\Delta\beta_2 = 0.05$  by means of the constraint on the quadrupole moment  $q_{20}$ . The calculations are performed by successive diagonalizations using the method of quadratic constraints [79]. The parallel version of the computer code allows simultaneous calculations for a significant number of nuclei and deformation points in each nucleus. For each nucleus, we minimize

$$E_{\text{quad}} = E_{\text{RHB}} + C_{20}(\langle \hat{Q}_{20} \rangle - q_{20})^2 \quad (9)$$

where  $E_{\text{RHB}}$  is the total energy and  $\langle \hat{Q}_{20} \rangle$  denotes the expectation value of the mass quadrupole operator,

$$\hat{Q}_{20} = 2z^2 - x^2 - y^2; \quad (10)$$

$q_{20}$  is the constrained value of the multipole moment; and  $C_{20}$  the corresponding stiffness constant [79]. In order to provide the convergence to the exact value of the desired multipole moment we use the method suggested in Ref. [80]. Here the quantity  $q_{20}$  is replaced by the parameter  $q_{20}^{\text{eff}}$ , which is automatically modified during the iteration in such a way that we obtain  $\langle \hat{Q}_{20} \rangle = q_{20}$  for the converged solution. This method works well in our constrained calculations.

- (2) In addition, reflection-asymmetric (octupole deformed) constrained axial RHB calculations (RA-RHB) are performed in discussed below cases using a parallel version of the code developed in Ref. [48]. In these calculations, the constraint

$$E_{\text{quad}} + C_{30}(\langle \hat{Q}_{30} \rangle - q_{30})^2 \quad (11)$$

is employed in addition to the constraint on quadrupole moment [see Eq. (9)]. Here  $\langle \hat{Q}_{30} \rangle$  denotes the expectation value of the mass octupole operator:

$$\hat{Q}_{30} = z(2z^2 - 3x^2 - 3y^2). \quad (12)$$

Note that we also fix the (average) center of mass of the nucleus at the origin with the constraint

$$\langle \hat{Q}_{10} \rangle = 0 \quad (13)$$

on the center-of-mass operator  $\hat{Q}_{10}$  in order to avoid a spurious motion of the center of mass. In the present paper, reflection asymmetric RHB calculations have been performed for the ground states of the nuclei



not covered in previous systematic studies of octupole deformation in CDFT (see Refs. [48,61]). We have not found any additional (as compared with those given in Refs. [48,61]) nuclei which possess octupole deformation in the ground state. So full information on the octupole deformation of the ground states can be found in these references. The information (which follows from Refs. [48,61]) about the gain in binding energy due to octupole deformation at the ground state and its impact on ground-state quadrupole deformation and fission barrier heights is fully taken into account in the present paper. In addition, RA-RHB calculations have been performed in some nuclei in order to define the heights of outer fission barriers (see the discussion below for more details).

The charge quadrupole and octupole moments are defined as

$$Q_{20} = \int d^3r \rho(\mathbf{r}) (2z^2 - r_{\perp}^2), \quad (14)$$

$$Q_{30} = \int d^3r \rho(\mathbf{r}) z(2z^2 - 3r_{\perp}^2) \quad (15)$$

with  $r_{\perp}^2 = x^2 + y^2$ . In principle these values can be directly compared with experimental data. However, it is more convenient to transform these quantities into dimensionless deformation parameters  $\beta_2$  and  $\beta_3$  using the relations

$$Q_{20} = \sqrt{\frac{16\pi}{5}} \frac{3}{4\pi} ZR_0^2 \beta_2, \quad (16)$$

$$Q_{30} = \sqrt{\frac{16\pi}{7}} \frac{3}{4\pi} ZR_0^3 \beta_3 \quad (17)$$

where  $R_0 = 1.2A^{1/3}$ . These deformation parameters are more frequently used in experimental works than quadrupole and octupole moments. In addition, the potential-energy surfaces (PESs) are plotted in this paper in the  $(\beta_2, \beta_3)$  deformation plane.

Because of different patterns of deformation energy curves (see Figs. 2 and 3), a special care is used when assigning a specific minimum to the ground state. A basic rule in this process is the assumption that the local minimum surrounded by the barrier, the height of which is less than 2 MeV, is considered as extremely unstable.<sup>4</sup> The procedure of the selection of the ground state is discussed below. The situation shown in Fig. 4(a) is the simplest one: a single-humped (inner) fission barrier acts against the fission into two fragments and when  $B_{\text{in}} > 2$  MeV the assignment of the normal-deformed prolate minimum to the ground state is straightforward. It changes if the height of this fission barrier decreases and becomes

smaller than 2 MeV [see Fig. 4(b)]. Then highly deformed oblate minimum B becomes a ground state; it has a larger and broader fission barrier as compared with minimum A. Thus, it is expected that this ground state will live significantly longer than the state associated with minimum A.

A more complex situation involving two humped fission barriers is shown in Fig. 4(c). If  $B_{\text{out-iso}} < 2$  MeV, then the minimum B corresponding to the fission isomer is considered extremely unstable and the minimum A is associated with the ground state. Note that in some cases the minimum B can be lower in energy than minimum A. If that is the case and if  $B_{\text{out-iso}} > 2$  MeV then the minimum B is considered as the ground state. Note that the heights of outer fission barriers are frequently lowered when octupole deformation is included in the calculations [63,69,78,81–83]. Thus, if  $B_{\text{out-iso}} > 2$  MeV in RS-RHB calculations, we perform RA-RHB calculations in the region of the  $(\beta_2, \beta_3)$  plane covering the minimum B and the saddle of the outer fission barrier on the grid with the steps of  $\Delta\beta_2 = \Delta\beta_3 = 0.05$ . This allows us to establish whether minimum B could be considered as relatively stable or unstable. Similar calculations are also performed in the cases when  $B_{\text{in}} < B_{\text{out}}$  in the RS-RHB calculations. This is because we consider only the height of the primary (highest) fission barrier in Sec. V in the case of a doubly humped structure of the barrier to minimize the computational cost. Note that the calculations leading to the definition of the fission path and the saddle point in the RA-RHB code are by roughly two orders of magnitude more time consuming than those in the RS-RHB code.

The procedure outlined above takes into account potential stability of the nuclei in respective energy minima with respect to fission and it is especially important in superheavy nuclei some local minima of which are characterized by small fission barriers (see Fig. 2). Note that after defining the minimum corresponding to the ground state the RS-RHB and RA-RHB calculations without constraint are performed in it and precise binding energy and equilibrium of the ground state are determined. In addition, the height(s) of the fission barrier(s) is(are) defined.

In the calculations with the PC-PK1 and NL3\* functionals there are two small islands of the nuclei located in the  $Z \approx 114\text{--}118$ ,  $N \approx 238\text{--}240$  and  $Z \approx 106\text{--}110$ ,  $N \approx 190\text{--}194$  regions in which calculated deformation energy curves reveal several local minima [somewhat similar to the deformation energy curves shown at the bottom of Fig. 2(b)]. However, all these minima are surrounded by very low fission barriers with the heights smaller than 2.0 MeV. Moreover, many of these minima have even lower heights of respective fission barriers (on the level of 1.0 MeV or smaller). These nuclei are expected to be unstable against fission and in principle it does not matter which of the calculated fission barriers is used. For these nuclei, we select the ground state guided by the flow of the  $\beta$  decays in the  $r$  process: the selected local minimum (and thus the corresponding ground-state deformation and fission barrier height) in the  $(Z, N)$  nucleus has the deformation closest to the one of the well-established ground state in the  $(Z - 2, N + 2)$  nucleus.

So far all existing global calculations of the fission barriers for the  $r$ -process simulations have been performed in

<sup>4</sup>This low fission barrier of 2 MeV or less would translate into a high penetration probability for spontaneous fission so that such minima are expected to be extremely unstable. In addition, the inclusion of octupole deformation (or triaxial deformation in some nuclei [78]) in the case of superdeformed minima surrounded by such low fission barriers could either completely eliminate or substantially reduce them (see Refs. [66,78,81]).

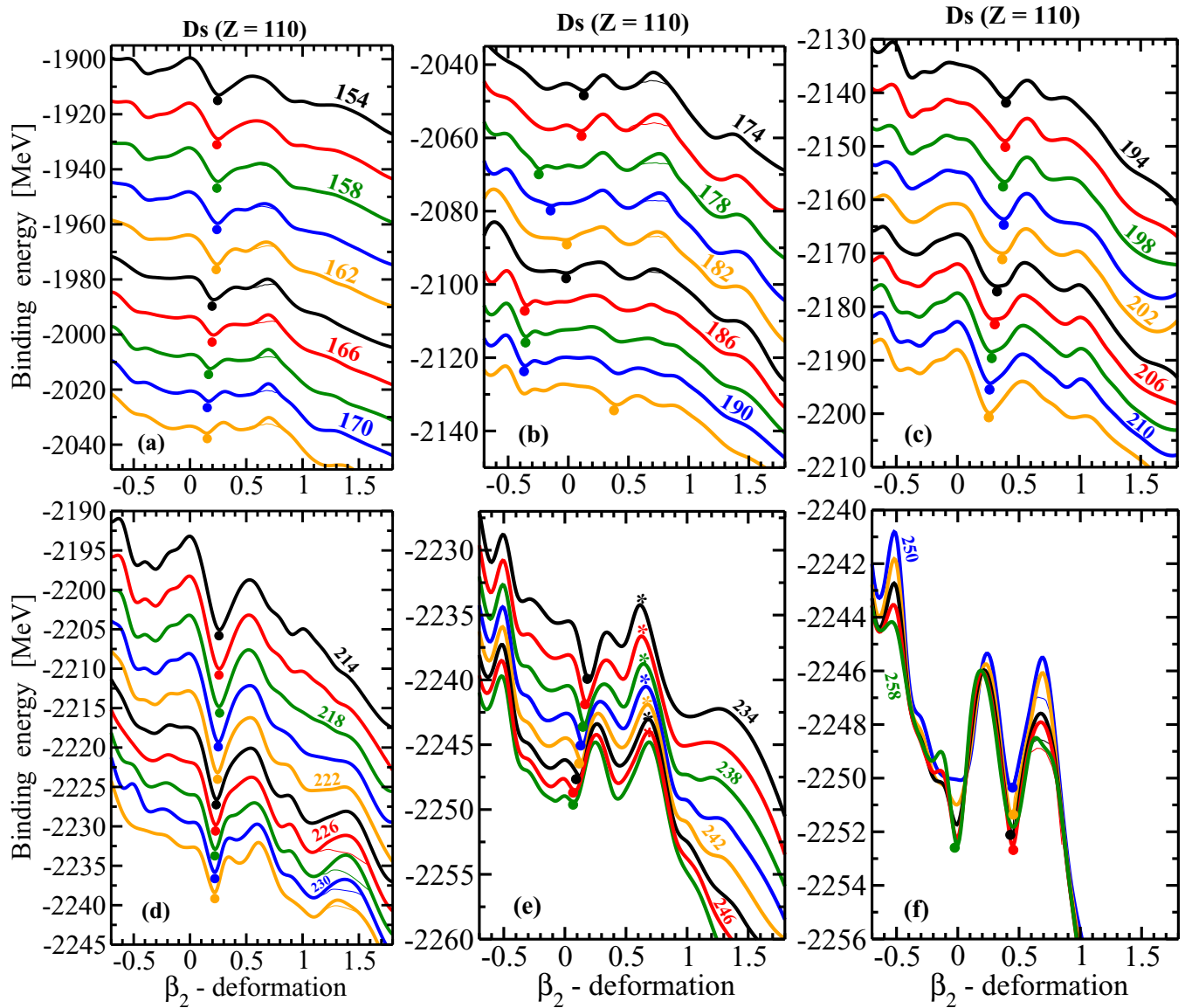


FIG. 2. Deformation energy curves obtained in axial RHB calculations with the DDPC1 functional for the Ds isotopes. The isotopes are indicated by respective neutron numbers. Thick and thin solid lines are used for the RS-RHB and RA-RHB results, respectively. The results of the RA-RHB calculations are shown only in the deformation range in which they are lower in energy than the RS-RHB ones. Solid circles indicate the ground states and the asterisks denote the saddles of outer fission barriers which are not affected by octupole deformation. Blue, orange, black, red, and green lines are used to indicate neutron numbers the last digits of which are 0, 2, 4, 6, and 8, respectively. Note that the energy on the vertical axis spans different ranges in different panels.

nonrelativistic models. These include the calculations within the FRDM [18,84], the TF and ETFSI-Q approaches [15,19], the HFB approaches with different Skyrme functionals [21,22,85], Gogny DIM\* [23], and BCPM [18] EDFs. Because of their global character, all these calculations are restricted to axial symmetry. We also assume axial symmetry in our calculations because triaxial RMF+BCS and RHB calculations (see Refs. [47,62,66,78,86]) are too time consuming to be performed on a global scale. Note also that dynamical correlations are not taken into account in our calculations of fission barriers because of the reasons discussed in Appendix A.

### III. GROUND-STATE PROPERTIES

The distributions of calculated proton deformations  $\beta_2$  in the  $(Z, N)$  plane obtained with four employed CEDFs are shown in Fig. 5. The width of the gray region (the gray color corresponds to spherical and near-spherical shapes) along a specific magic number corresponding to a shell closure indicates the impact of this shell closure on the structure of neighboring nuclei. Note that proton and neutron shell gaps act simultaneously in the vicinity of doubly magic spherical nuclei. Thus, the effect of a single gap is more quantifiable away from these nuclei. One can see that neutron  $N = 184$

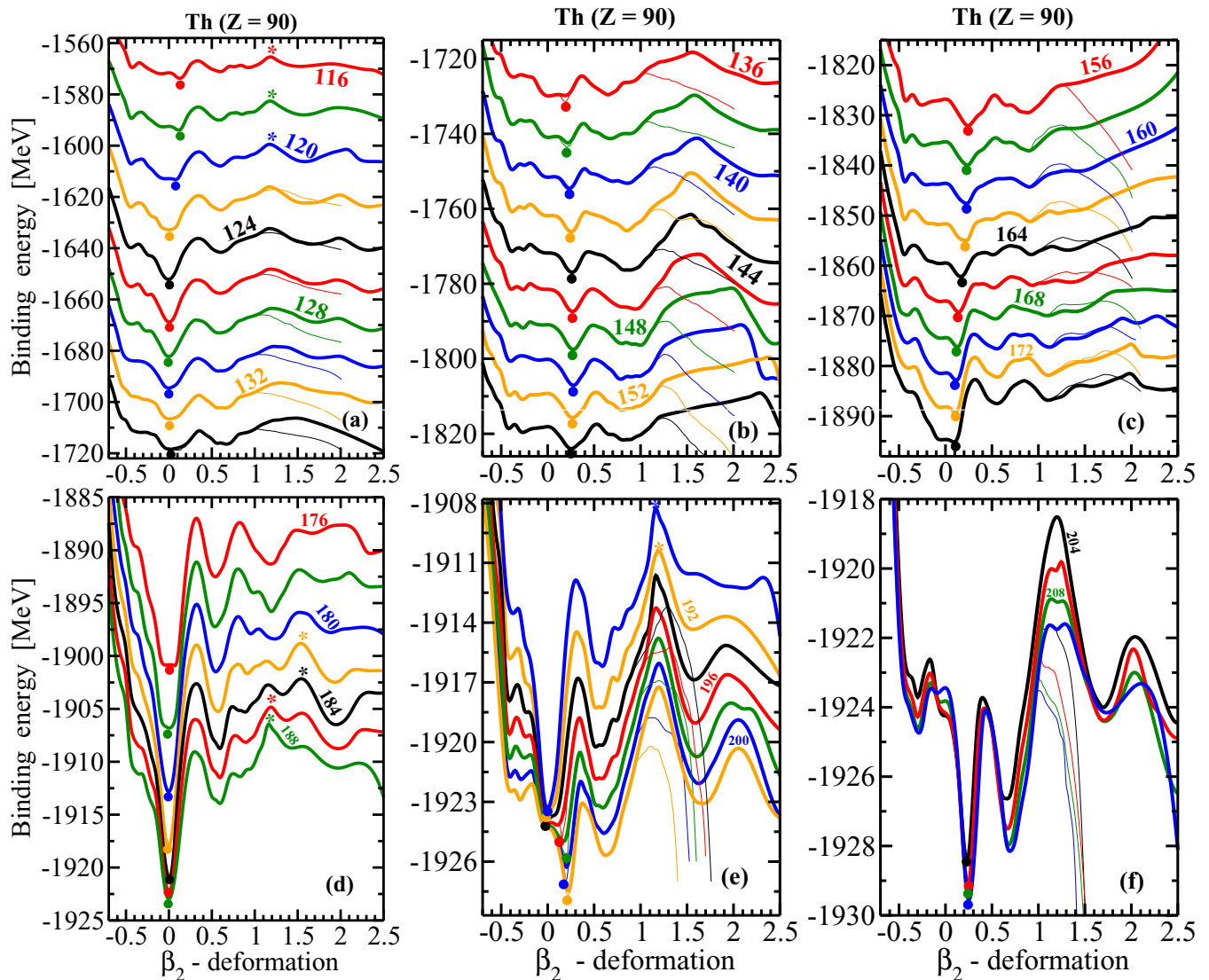


FIG. 3. The same as Fig. 2 but for the Th isotopes. Note that the deformation range has been extended on the horizontal axis as compared with Fig. 2. In order to save computational time the RA-RHB calculations have been carried out only up to  $\beta_2 = 2.0$ .

and 258 spherical shell gaps<sup>5</sup> have a pronounced impact on calculated deformations while the impact of the proton  $Z = 120$  spherical shell closure is limited to the  $N \sim 170$ – $184$  nuclei (see Refs. [59,90] for examples of their size dependence on the functional). In addition, as illustrated in Ref. [86] on the example of the PC-PK1 functional, the inclusion of the correlations beyond mean field washes out the impact of the  $Z = 120$  shell closure and leads to oblate deformed ground states in the majority of the  $Z = 120$  nuclei with  $N = 172$ – $186$ .

<sup>5</sup>Note that appreciable  $N = 258$  spherical shell gap appears also in the calculations of some superheavy nuclei with other CEDFs such as G1, G2 [87], NL3 [87–89], NL-Z2 [88], NL1, NLSH, TM1, TW99, DD-ME1, PK1, and PK1R [89]. However, these calculations are restricted to spherical shapes and thus it is not clear how large is the impact of this gap on ground-state deformations in the region near the  $N = 258$  line.

The predictions of the DD-PC1 functional differ substantially from other CEDFs: the impact of above-mentioned shell closures are substantially reduced in it and as a consequence the regions with  $Z \sim 120$ ,  $N \sim 184$  and  $Z \sim 120$ ,  $N \sim 258$  are dominated by oblate ground states contrary to spherical states in other functionals. Note that this functional provides the best global description of experimental binding energies (see Ref. [39]). This, however, does not guarantee that it will outperform other functionals in the description of physical observables of interest in the region of superheavy nuclei (see Table I in Ref. [59]).

The calculations reveal a number of nuclei scattered across the part of the nuclear chart under study which have extremely superdeformed (ESD) minima with  $\beta_2 \sim 1.0$  located at lower energy than normal-deformed minima [see Fig. 6(a) and Table I]. In these nuclei the ESD minimum is surrounded by an outer fission barrier the height of which exceeds 2.0 MeV (being typically in the range of 2.0–3.0 MeV) in the RA-RHB

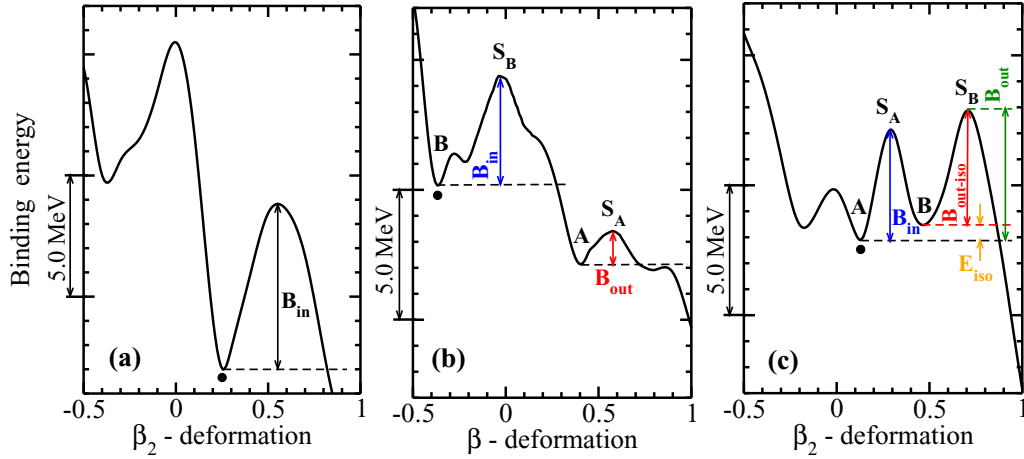


FIG. 4. Schematic illustration of different types of deformation energy curves and the selection of respective ground states (see text for details). Local minima are labeled by the letters A and B and the saddle points of respective fission barriers are labeled by  $S_A$  and  $S_B$ . Solid circles indicate the minima selected as the ground states. The heights of inner and outer fission barriers with respect of corresponding minima (shown by dashed lines) are indicated by  $B_{in}$  and  $B_{out}$ .  $B_{out-iso}$  is the height of the outer fission barrier with respect to the fission isomer.

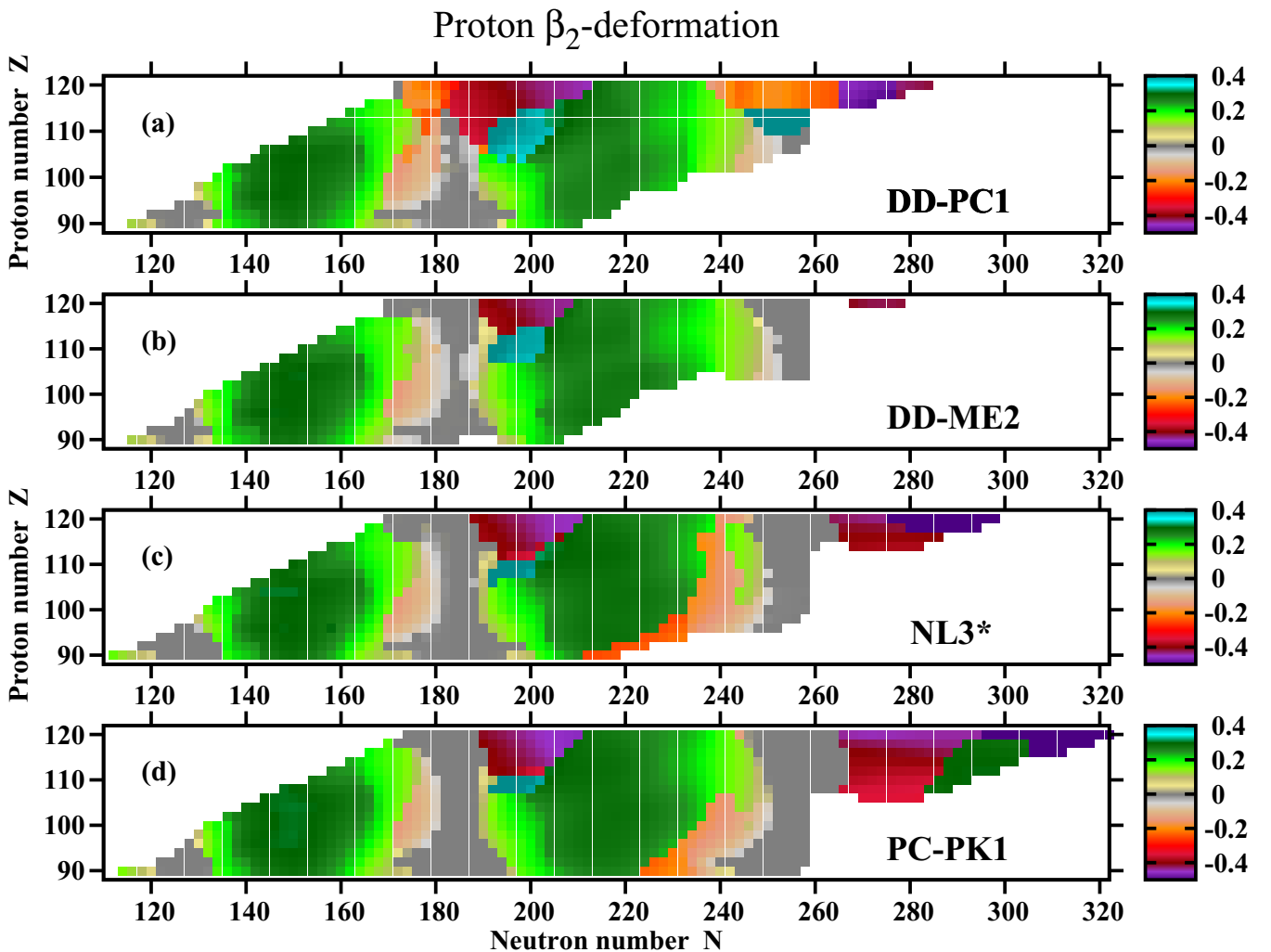


FIG. 5. Proton quadrupole deformations  $\beta_2$  obtained in the RS-RHB and RA-RHB calculations with indicated CEDFs (see Refs. [48,61] for the details of the regions of octupole deformation). Note that the last bound  $Z = 120$  nucleus appears at  $N = 324$  in the calculations with the CEDF PC-PK1 (see Table III below); for simplicity it is not shown in panel (d).



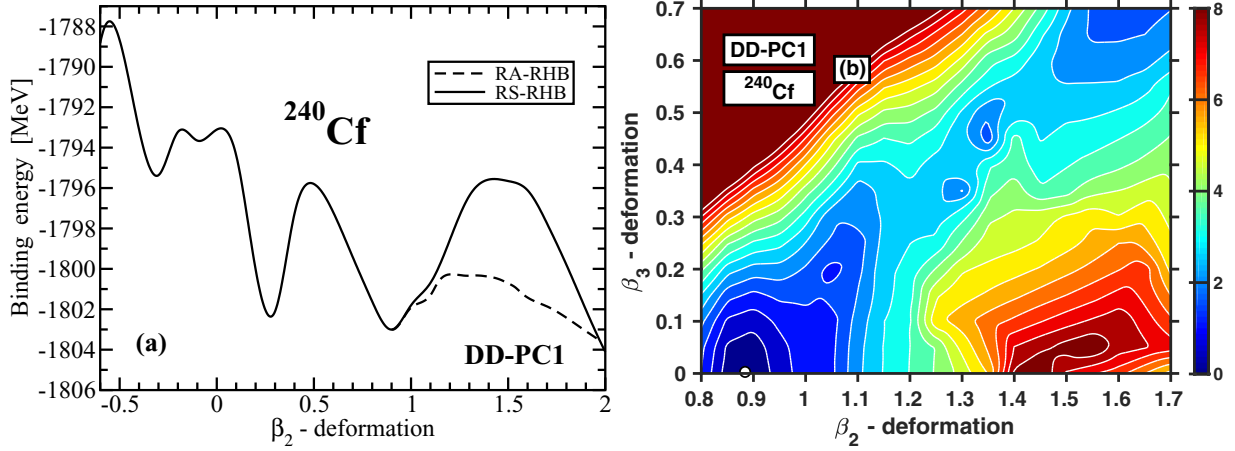


FIG. 6. (a) Deformation energy curves obtained in axial RS-RHB calculations with the CEDF DD-PC1 for the  $^{240}\text{Cf}$  nucleus. (b) Potential-energy surface in the  $(\beta_2, \beta_3)$  plane obtained in the RA-RHB calculations. The extremely superdeformed minimum is indicated by the open white circle.

calculations [see Fig. 6(b) and Table I]. Although the fission barrier is low, some of these ESD minima could be potentially stabilized against fission for physically sufficient time because

TABLE I. The nuclei in which the extremely superdeformed minimum is the lowest in energy in the calculations with CEDF DD-PC1. The columns 1 and 2 show the proton and neutron numbers of the nuclei. The third column displays the energy  $E_{N-S}$  (in MeV) by which the ESD minimum is lower than the normal-deformed minimum. The deformations of the ESD minimum  $\beta_2^{\text{min}}$  and the saddle of second fission barriers  $\beta_2^{\text{saddle}}$  and  $\beta_3^{\text{saddle}}$  are presented in the columns 4 and 5, respectively. The energies (in MeV) of the second fission barrier with respect to the ESD minimum, obtained in the RS-RHB and RA-RHB calculations, are shown in the columns 6 and 7. Note that the values presented in the columns 5–7 are obtained in the calculations with  $N_F = 26$ ; this is done in order to have a comparable numerical accuracy with the one obtained at normal deformed minimum.

Z	N	$E_{N-S}$ (MeV)	$\beta_2^{\text{min}}$	$\beta_2^{\text{saddle}}, \beta_3^{\text{saddle}}$	$E_B^{\text{II}}$ (MeV) (RS-RHB)	$E_B^{\text{II}}$ (MeV) (RA-RHB)
1	2	3	4	5	6	7
98	142	0.603	0.88	1.21, 0.33	7.207	2.625
98	144	0.306	0.90	1.34, 0.46	7.373	3.503
98	228	2.341	1.01	1.29, 0.34	6.622	2.906
98	230	2.083	1.01	1.30, 0.35	5.072	3.203
100	146	0.876	0.97	1.32, 0.37	5.890	2.985
100	230	2.431	1.01	1.30, 0.35	5.750	3.270
100	232	2.336	1.01	1.30, 0.37	4.060	2.739
102	146	2.038	0.99	1.32, 0.34	4.813	2.749
102	148	0.629	0.98	1.28, 0.31	4.093	2.250
102	232	2.591	1.02	1.29, 0.36	3.476	2.840
102	234	3.567	1.03	1.31, 0.31	2.674	2.304
104	146	3.435	0.99	1.33, 0.28	6.042	2.410
104	148	1.921	1.00	1.31, 0.27	5.579	2.204
104	150	0.924	1.00	1.29, 0.27	5.370	2.505
106	148	3.638	1.08	1.32, 0.26	4.112	2.340
106	150	2.374	1.10	1.30, 0.23	3.753	2.345

of the broad fission barrier in the  $(\beta_2, \beta_3)$  plane. If this were the case, they would represent the ground states. However, they are not included in Fig. 5 because of the following reasons. First, there are significant theoretical uncertainties in the predictions of fission barriers (see the present paper and Refs. [47,78]) as well as in relative energies of the minima with different deformations [73]. Second, only a few nuclei in the  $Z \approx 100, N \approx 230$  region could be potentially extremely superdeformed in the ground states (see Table I). However, the flow of matter in the  $r$  process between two nuclei with drastically different deformations of the ground states will be most likely significantly suppressed because of considerable differences in the wave functions of these ground states. Thus, it will proceed mostly along the dominant deformation of the ground states in the region, namely, normal deformation, even if such states are excited in energy in a few nuclei. Third, the majority of the nuclei in Table I are neutron poor  $Z \approx 102$  nuclei which do not play a role in the  $r$  process. There are experimental data on the  $^{240,242}\text{Cf}$ ,  $^{246}\text{Fm}$ , and  $^{254}\text{Rf}$  nuclei but only for their ground states [91]. At present, these data do not allow us to define the deformations of the ground states. However, since they have been obtained in the reactions (such as  $\alpha$  decay,  $\beta$  decay, electron capture, and the reactions on spherical Pb isotopes) which do not favor significant shape changes, these ground states are most likely normal-deformed. More detailed and focused experimental studies are needed in order to see whether ESD states exist in such nuclei.

The spreads of theoretical predictions in quadrupole deformations  $\beta_2$  obtained with four employed functionals are summarized in Fig. 7(a). The largest spread of  $\Delta\beta_2 \approx 0.7$  is visible along the line of  $N/Z \approx 1.81$  which starts at  $Z = 104$ . This corresponds to the boundary of the transition from oblate to prolate shapes the exact position of which in the  $(Z, N)$  plane is functional dependent (see Fig. 5). It is defined by the underlying single-particle structure at prolate and oblate shapes as well as to a degree by the heights of outer fission barriers (see the rules for the definition of the ground states described in Sec. II). The second region of the largest spreads in  $\Delta\beta_2$  is located along the  $N \approx 184$  line starting from  $Z \approx 100$

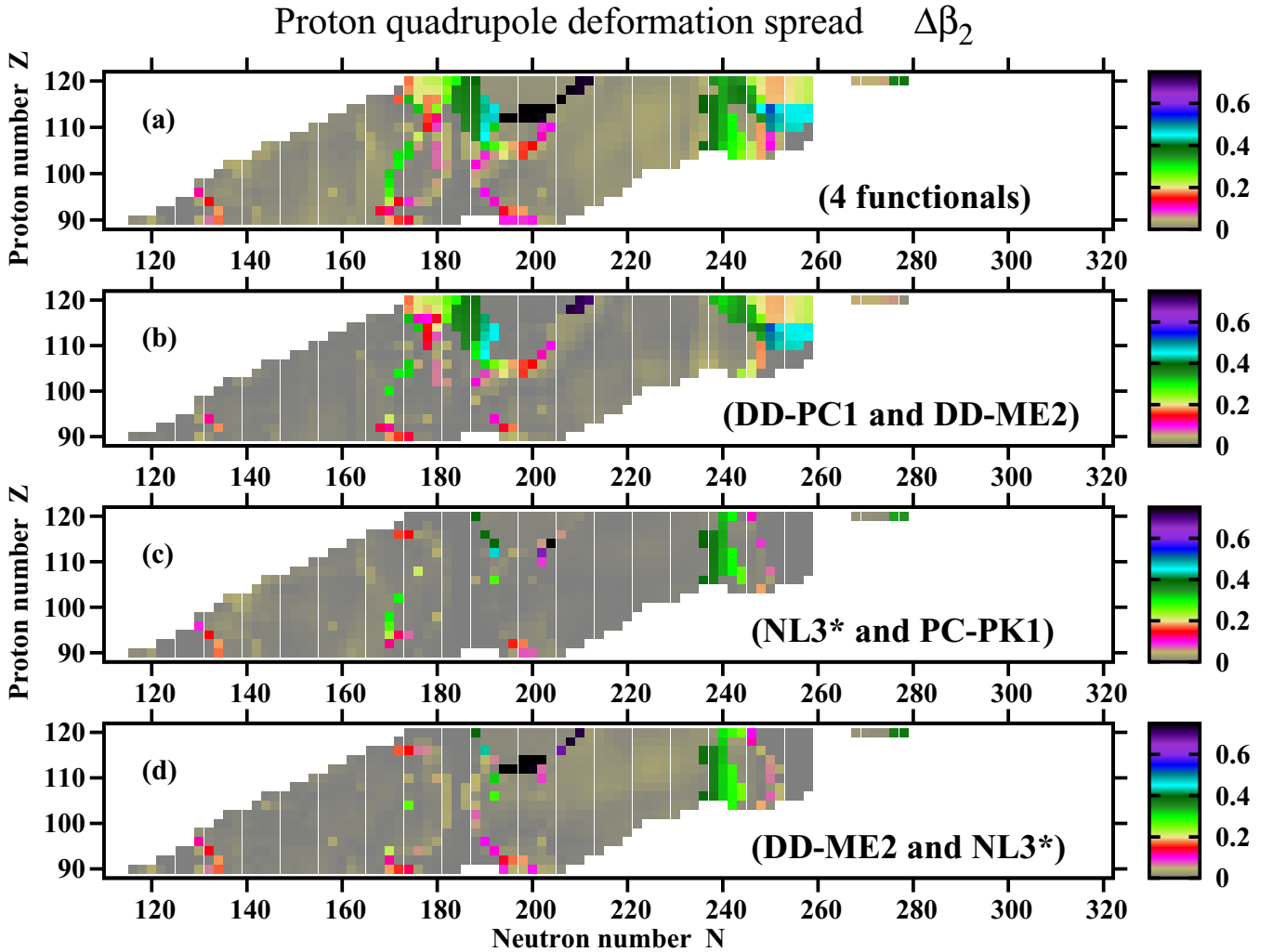


FIG. 7. Proton quadrupole deformation spreads  $\Delta\beta_2(Z, N)$  as a function of proton and neutron number.  $\Delta\beta_2(Z, N) = |\beta_2^{\max}(Z, N) - \beta_2^{\min}(Z, N)|$ , where  $\beta_2^{\max}(Z, N)$  and  $\beta_2^{\min}(Z, N)$  are the largest and smallest proton quadrupole deformations obtained with four employed CEDFs for the  $(Z, N)$  nucleus.

and extending up to  $Z = 120$ . The third region is located along the  $Z = 120$  line from the proton drip line up to  $N \approx 188$ . These two regions of large spreads in calculated quadrupole deformation emerge from the differences in the predictions of ground-state deformations (see Fig. 5) which in turn can be traced back to the sizes of the  $Z = 120$  and  $N = 184$  spherical shell closures and the densities of the single-particle states in their vicinities (see Ref. [59]). The last region of large theoretical uncertainties is located between  $N \approx 236$  and  $N = 258$ . In the region around  $N \approx 236$  these theoretical uncertainties are mostly due to the uncertainties in the predictions of the boundary of the transition from prolate to oblate shapes. For higher  $N$  values, large  $\Delta\beta_2$  values emerge from the transition from prolate or oblate shapes to spherical ones and to a large degree are defined by the uncertainties in the prediction of the size of the  $N = 258$  spherical shell closure [see Fig. 6(d) in Ref. [90]] and single-particle densities in its vicinity. With few exceptions theoretical uncertainties in the predictions of ground-state deformations in the part of the nuclear chart

outside of the above-discussed regions are very small [see Fig. 7(a)].

It is important to understand to what extent the predictions of the ground-state deformations and related theoretical uncertainties in these predictions are dependent on nuclear matter properties of employed CEDFs. All employed CEDFs have the density  $\rho_0$  and the energy per particle  $E/A$  at the saturation of symmetric nuclear matter (SNM) which are very close to each other and to empirical estimates (see Table III in Ref. [49]). Thus, the impacts of only selected SNM properties listed in Table II on the ground-state deformations are discussed below. Let us start from the consideration of the predictions by the pair of the functionals DD-PC1 and DD-ME2. Their SNM properties such as incompressibility  $K_0$ , symmetry energy  $J$ , and slope  $L_0$  are close to each other and are located within the SET2b constraints on experimental/empirical ranges for physical observables of interest (see Table II). Despite that this pair of functionals gives the largest contribution into the spreads  $\Delta\beta_2$  [compare panels (b) and (a) of Fig. 7].

TABLE II. Selected properties of symmetric nuclear matter at saturation: the incompressibility  $K_0$ , the symmetry energy  $J$ , and its slope  $L_0$ . The top four lines show the values for indicated CEDFs, while the bottom two lines show two sets (SET2a and SET2b) of the constraints on the experimental/empirical ranges for the quantities of interest defined in Ref. [51]. The CEDF values which are located outside the limits of the SET2b constraint set are shown in bold.

CEDF	$K_0$ (MeV)	$J$ (MeV)	$L_0$ (MeV)
1	2	3	4
NL3* [43]	258	<b>38.68</b>	<b>122.6</b>
DD-ME2 [42]	251	32.40	49.4
DD-PC1 [44]	230	33.00	68.4
PC-PK1 [50]	238	<b>35.6</b>	<b>113</b>
SET2a	190–270	25–35	25–115
SET2b	190–270	30–35	30–80

In contrast, the pairs of functionals PC-PK1 and NL3\* [which have  $J$  and  $L_0$  values located outside the SET2b constraint range (see Table II)] as well as NL3\* and DD-ME2 [which have drastically different values of the  $J$  and  $L_0$  parameters (see Table II)] have (with very few exceptions) very similar predictions for the ground-state deformations across the part of the nuclear chart under study. These exceptions are related to some differences in the predictions of the boundaries between oblate and prolate shapes as well as between prolate and spherical shapes.

These results for ground-state deformations together with the analysis of the results for binding energies and charge radii of the  $Z \leq 104$  nuclei presented in Ref. [49] strongly indicate the following.

- (1) The major source of the uncertainties in the predictions of ground-state deformations is related to local differences in underlying single-particle structure and, in particular, to the size of spherical  $Z = 120$  and  $N = 184$  and  $258$  shell closures and the densities of the single-particle states in their vicinities.
- (2) Strict enforcement of the limits on the nuclear matter properties defined in Ref. [51] will not necessary lead to the functionals with good description of ground- and excited-state properties and will not reduce theoretical uncertainties in the description of physical observables of interest in high- $Z$  and/or neutron-rich nuclei.

Table III compares the positions of the two-proton and two-neutron drip lines obtained in the RHB calculations with the NL3\* and PC-PK1 functionals; the results for the DD-PC1 and DD-ME2 functionals could be found in Table IV of Ref. [39]. One can see that the two-proton drip lines are very similar in these two functionals; they differ by no more than four neutrons. This is in line with earlier observations that theoretical uncertainties in the predictions of the position of the two-proton drip line are relatively small (see Ref. [93] and Sec. VII in Ref. [39]). Note that two-proton drip lines in the isotopic chains of interest obtained with PC-PK1 are very close to those obtained with DD-PC1 (compare Table III in the present paper with Table IV of Ref. [39]).

TABLE III. Two-proton and two-neutron drip lines predicted by the NL3\* and PC-PK1<sup>a</sup> functionals (see Fig. 1 for a graphical representation of drip lines). Neutron numbers (columns 2–5) corresponding to these drip lines are given for each even proton number  $Z$  (column 1). An asterisk at a neutron number at the two-neutron drip line indicates isotope chains with additional two-neutron binding at higher  $N$  values (peninsulas).

Proton number $Z$	Two-proton drip line		Two-neutron drip line	
	NL3*	PCPK1	NL3*	PCPK1
1	2	3	4	5
90	112	114	218	256
92	118	122	224	258
94	122	126	232	258
96	126	128	252	258
98	130	130	256	258
100	132	132	258	258
102	134	136	258	258
104	138	140	258	258
106	142	144	258	258*
108	146	148	258	288
110	150	154	258	292
112	154	158	258	298
114	158	162	262*	302
116	162	166	286	312
118	166	170	294	318
120	170	174	298	324

<sup>a</sup>The analysis of Ref. [92] performed within the relativistic continuum Hartree-Bogoliubov theory and PC-PK1 functional leads to somewhat different predictions for the position of the two-neutron drip line for some isotopic chains as compared with our results. This is a consequence of the neglect of deformation effects in Ref. [92].

Among the considered CEDFs the PC-PK1 functional provides the most neutron-rich two-neutron drip line and the NL3\* provides the second most neutron-rich two-neutron drip lines (compare Table III in the present paper with Table IV of Ref. [39] and see Sec. VIII in Ref. [39]). All employed functionals reveal the presence of the shell closure at  $N = 258$  [see Fig. 6(d) in Ref. [90]]. The size of this gap is almost the same in the NL3\* and PC-PK1 functionals, but (i) it is shifted down in energy by  $\approx 400$  keV for PC-PK1 as compared with NL3\* and (ii) high- $j$  intruder orbitals  $1k_{15/2}$  and  $2i_{13/2}$ , which have a significant impact on the position of the neutron drip line (see discussion in Ref. [90]), are located at lower energies in the PC-PK1 functional as compared with the NL3\* one. These features lead to the shift of the two-neutron drip line to substantially higher neutron numbers in the PC-PK1 CEDF as compared with NL3\*. The sizes of the  $N = 258$  shell gaps are smaller by  $\approx 10$  and  $20\%$  in the DD-ME2 and DD-PC1 functionals as compared with the ones in the PC-PK1 and NL3\*. In addition, above-mentioned high- $j$  intruder orbitals in the calculations with the DD-ME2 and DD-PC1 functionals are located at higher energies as compared with the ones in NL3\*. As a consequence, their two-neutron drip lines are located at lower neutron numbers as compared with the NL3\*. These features are clearly seen in Fig. 5.

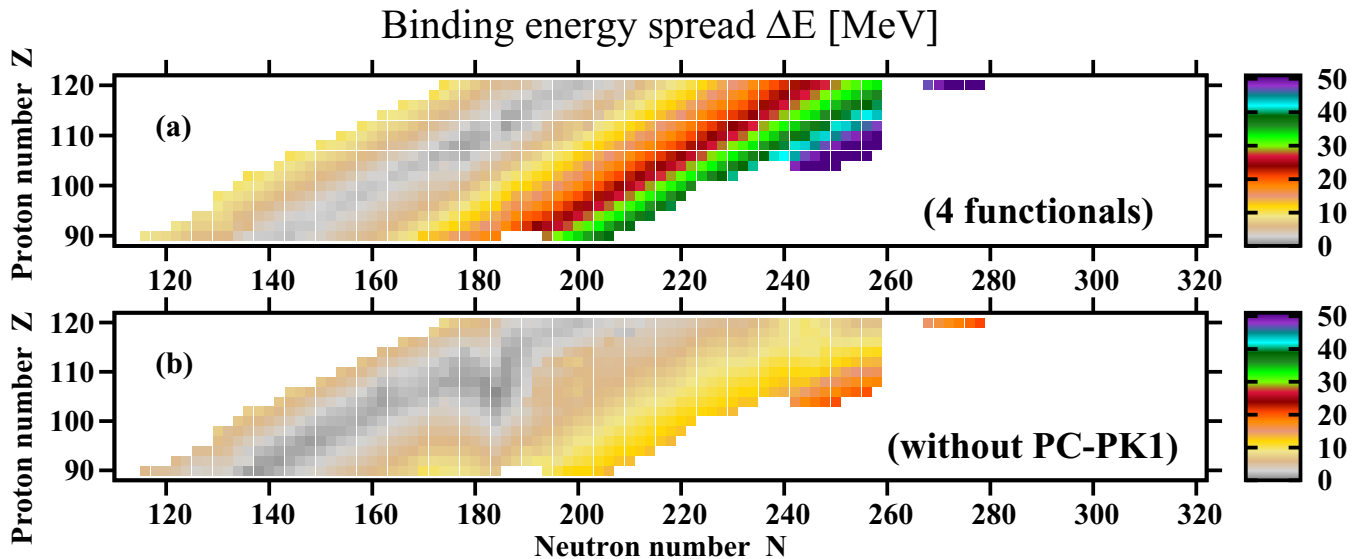


FIG. 8. The binding-energy spreads  $\Delta E(Z, N)$  as a function of proton and neutron number.  $\Delta E(Z, N) = |E_{\max}(Z, N) - E_{\min}(Z, N)|$ , where  $E_{\max}(Z, N)$  and  $E_{\min}(Z, N)$  are the largest and smallest binding energies obtained with the employed set of CEDFs for the  $(Z, N)$  nucleus. The upper panel shows the binding-energy spreads for four employed functionals, while the bottom one shows the spreads for a set of functionals in which PC-PK1 is excluded.

Figure 8 shows the map of theoretical uncertainties  $\Delta E(Z, N)$  in binding energies. These uncertainties increase drastically when approaching the neutron-drip line and in some nuclei they reach 50 MeV. Poorly defined isovector properties of CEDFs is the major reason for that (see Ref. [39]). Note that the  $\Delta E(Z, N)$  spreads for the NL3\*, DD-PC1, and DD-ME2 functionals are relatively modest [see Fig. 8(b)]<sup>6</sup> and the major contribution to  $\Delta E(Z, N)$  is coming from the PC-PK1 functional [compare panels (a) and (b) in Fig. 8]. The fact that isovector properties of the PC-PK1 functional are significantly different from those of NL3\*, DD-PC1, DD-ME2, and DD-ME $\delta$  is also confirmed by the analysis of binding energies in the Yb ( $Z = 70$ ) isotopic chain (see Fig. 3 in Ref. [49]). As follows from the analysis of parametric correlations in different classes of CEDFs performed in Ref. [58], a possible reason for that could be related to overparametrization of the isoscalar channel in this class of CEDFs.<sup>7</sup> This, in turn, may lead to a somewhat wrong balance of the isoscalar and isovector channels in known nuclei which reveals itself in a more pronounced way via different (as compared with other functionals) isovector dependence of binding energies in a neutron-rich one.

Figure 9 presents the summary of two-neutron separation energies  $S_{2n}(Z, N)$  obtained with four employed CEDFs. Note that some discontinuities in smooth trends of the  $S_{2n}(Z, N)$  distributions as a function of neutron number are either due to

the presence of substantial spherical shell gaps at  $N = 184$  or 258 or due to the crossing of the boundaries between prolate and oblate shapes. For example, the impact of the  $N = 184$  spherical shell gap on the  $S_{2n}(Z, N)$  distributions is clearly visible in Figs. 9(b)–9(d) [see also Figs. 5(b)–5(d) for deformation distributions]. In contrast, its impact is substantially suppressed in superheavy nuclei in the calculations with CEDF DD-PC1 [see Fig. 9(a)] because of the reduced role of the  $N = 184$  spherical shell gap in this functional.

Finally, the spreads  $\Delta S_{2n}(Z, N)$  in two-neutron separation energies are presented in Fig. 10. They are the lowest in known nuclei but in general increase with increasing neutron number. The  $\Delta S_{2n}(Z, N)$  values are quite large [ $\Delta S_{2n}(Z, N) \approx 2.2$  MeV] in the vicinity of two-neutron drip lines and the  $N = 184$  and 258 spherical shell gaps. However, they become extremely large [ $\Delta S_{2n}(Z, N) \approx 4.0$  MeV] at the boundaries between prolate and oblate shapes. Similar to the spreads in binding energies (see discussion of Fig. 8 above), the largest contribution to the  $\Delta S_{2n}(Z, N)$  values comes from the CEDF PC-PK1. If the PC-PK1 functional is excluded from consideration these values on average decrease by a factor of 2 [compare panels (b) and (a) in Fig. 10]. It is interesting that in the neutron-rich deformed  $N \approx 190$ –236 region the  $\Delta S_{2n}(Z, N)$  values are on average comparable with those in known nuclei [see Fig. 10(b)]. However, they still show increased magnitudes at above discussed locations of the nuclear chart.

#### IV. $\alpha$ -DECAY PROPERTIES

In actinides and superheavy nuclei spontaneous fission and  $\alpha$  emission compete and the shortest half-life determines the dominant decay channel and the total half-life. Only in the

<sup>6</sup>The addition of the DD-ME $\delta$  functional to this set of three functionals is not expected to modify significantly  $\Delta E(Z, N)$  (see Fig. 9 in Ref. [39]).

<sup>7</sup>The analysis of Ref. [58] suggests that the number of parameters in the isoscalar channel of PC-PK1 CEDF can be reduced from 4 to 1.



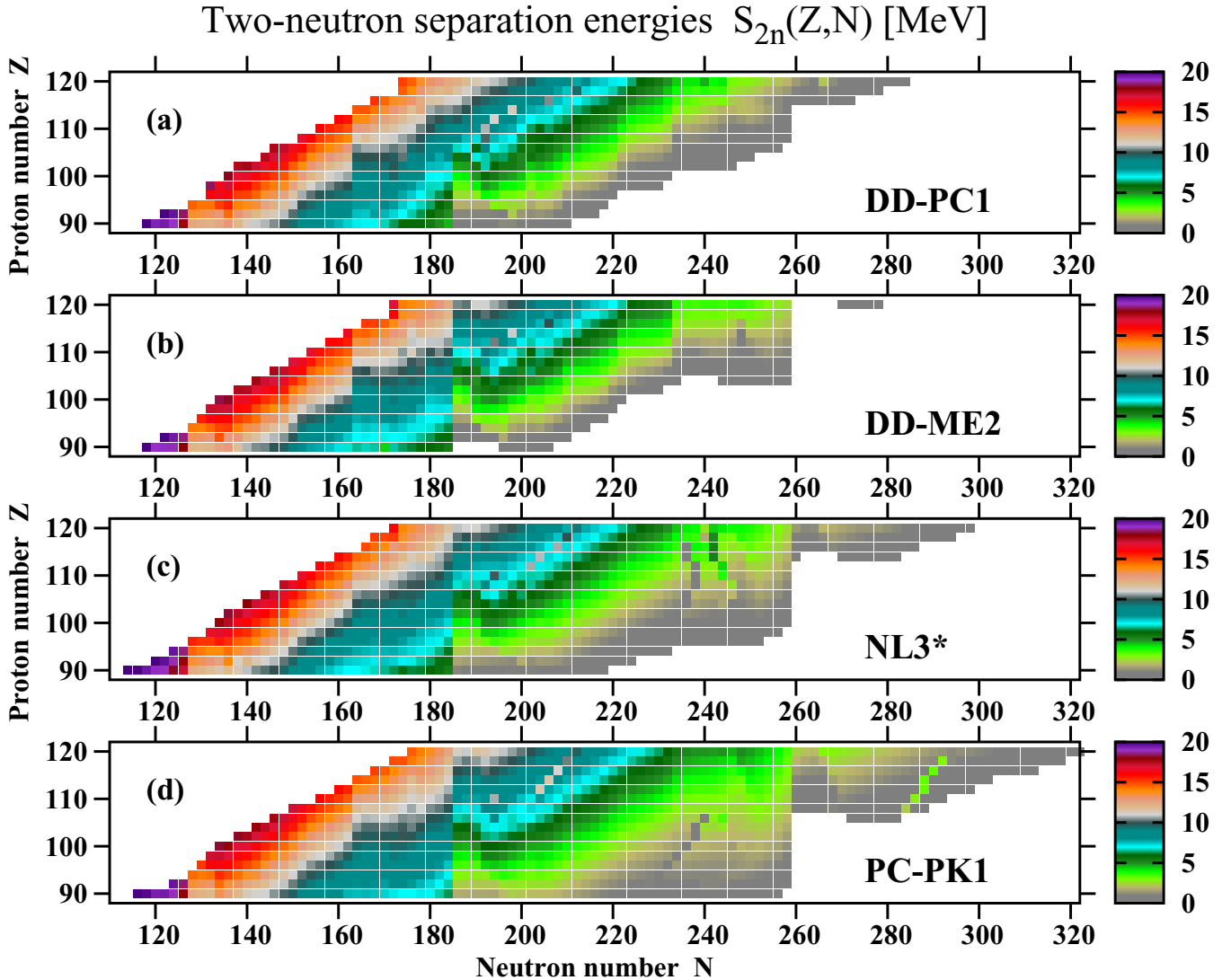


FIG. 9. Two-neutron separation energies  $S_{2n}(Z, N)$  obtained in the RHB calculations with indicated CEDFs.

cases where the spontaneous fission half-life is longer than the half-life of  $\alpha$  emission can superheavy nuclei be observed in experiment. In addition, only nuclei with half-lives longer than  $\tau = 10 \mu\text{s}$  are observed in experiments.

The  $\alpha$ -decay half-life depends on the  $Q_\alpha$  values which are calculated according to

$$Q_\alpha = E(Z, N) - E(Z - 2, N - 2) - E(2, 2) \quad (18)$$

with  $E(2, 2) = -28.295674$  MeV [94] and  $Z$  and  $N$  representing the parent nucleus.

To estimate theoretical uncertainties in the predictions of the  $\alpha$ -decay half-lives, they were calculated using three phenomenological expressions.

- (1) The first expression is the Viola-Seaborg semiempirical formula [95]

$$\log_{10}\tau_\alpha = \frac{aZ + b}{\sqrt{Q_\alpha}} + cZ + d \quad (19)$$

employing two sets of parametrizations. The first one with the parameters  $a = 1.66175$ ,  $b = -8.5166$ ,  $c = -0.20228$ , and  $d = -33.9069$  has been fitted in Ref. [96]. This set and the results obtained with it are labeled below as VSS-1989. Another set has been defined in Ref. [97] and its parameters are  $a = 1.64062$ ,  $b = -8.54399$ ,  $c = -0.19430$ , and  $d = -33.9054$ . The label VSS-2005 is used for it and its results.

- (2) The second expression is the phenomenological first modified Brown fit (mB1) [98]

$$\log_{10}\tau_\alpha = \frac{a(Z - 2)^b}{\sqrt{Q_\alpha}} + c \quad (20)$$

with the parameters  $a = 13.0705$ ,  $b = 0.5182$ , and  $c = -47.8867$ . This set and its results are labeled below as MB-2016.

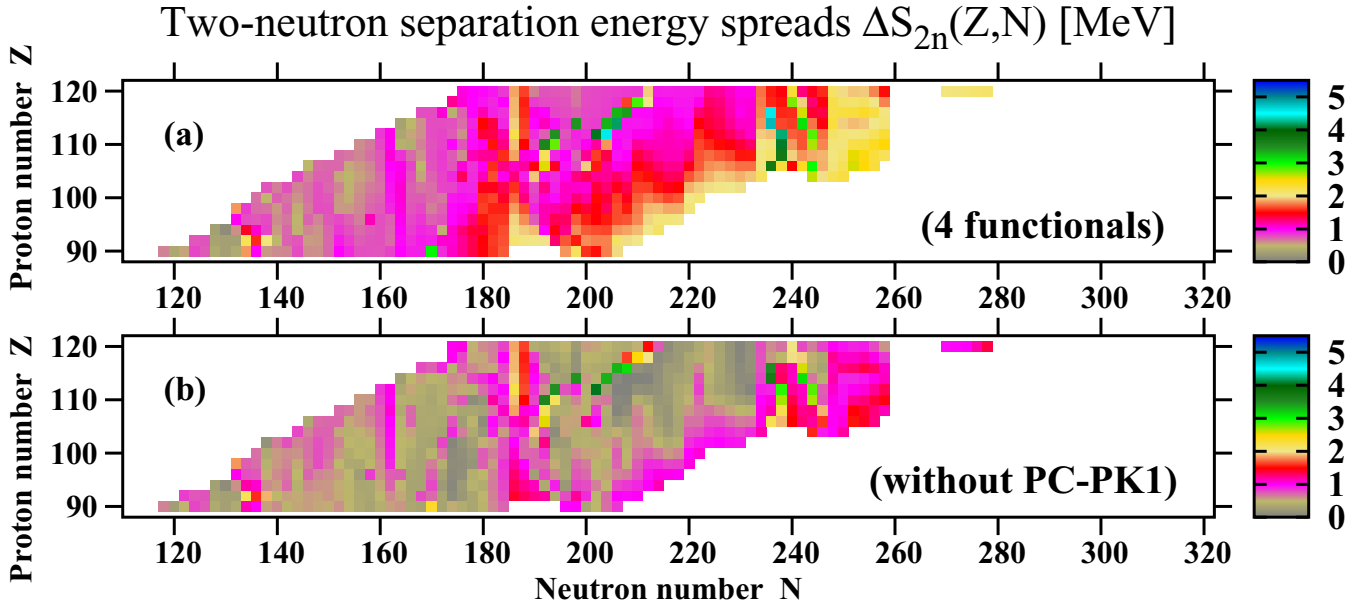


FIG. 10. The  $S_{2n}$  spreads  $\Delta S_{2n}(Z, N)$  as a function of proton and neutron number.  $\Delta S_{2n}(Z, N) = |S_{2n}^{\max}(Z, N) - S_{2n}^{\min}(Z, N)|$ , where  $S_{2n}^{\max}(Z, N)$  and  $S_{2n}^{\min}(Z, N)$  are the largest and smallest  $S_{2n}$  values obtained with four employed CEDFs for the  $(Z, N)$  nucleus.

- (3) The third expression is the phenomenological Royer model [99]

$$\log_{10} \tau_{\alpha} = \frac{aZ}{\sqrt{Q_{\alpha}}} + bA^{\frac{1}{6}} \sqrt{Z} + c \quad (21)$$

with the parameters  $a = 1.5864$ ,  $b = -1.1629$ , and  $c = -25.31$  of Ref. [99]. Its results are labeled below as Royer-2000.

These phenomenological expressions employ different functional dependencies (in particular, they show different dependencies on proton and mass numbers) and are fitted to different sets of experimental data. This is expected to lead to different predictions for  $\tau_{\alpha}$  in high- $Z$  and neutron-rich nuclei.

The  $Q_{\alpha}$  values calculated with the DD-PC1, DD-ME2, NL3\*, and PC-PK1 functionals are presented in Fig. 11. One can see that for a fixed value of  $Z$  with increasing neutron number the  $Q_{\alpha}$  values in general decrease. They are positive in proton-rich nuclei as well as in the nuclei located close to the  $\beta$ -stability line. The  $Q_{\alpha}$  values experience a substantial increase at shell closure with  $N = 184$ <sup>8</sup> (see Fig. 11 in the present paper as well as Fig. 14 in Ref. [59]); note that the effect of this shell closure is washed out in the  $Z > 110$  nuclei for the DD-PC1 functional. With subsequent increase of neutron number the  $Q_{\alpha}$  values become first smaller, then they become close (or equal) to zero, and with further increase of  $N$  they get more and more negative. Note that  $\alpha$  decay is energetically not possible for  $Q_{\alpha} \leq 0$  MeV. Thus, very neutron-rich nuclei cannot decay by  $\alpha$  emission.

Note that general trends in the development of the  $Q_{\alpha}$  values as a function of proton and neutron number are similar in all functionals. The major differences are related to the location of the two-neutron drip line, the impact of the  $N = 184$  and 258 shell closures, and the location of the boundaries between prolate and oblate nuclear shapes. These differences between the functionals are summarized in Fig. 12 which shows the  $Q_{\alpha}$  spreads  $\Delta Q_{\alpha}(Z, N)$  as a function of proton and neutron number. The largest spread in the predictions exists in the island centered around  $Z \sim 110, N \sim 198$  in which  $\Delta Q_{\alpha}(Z, N) > 3$  MeV. This spread emerges from different predictions of the boundaries in the  $(Z, N)$  plane between prolate and oblate shapes (see Fig. 5) and coincides with the largest spread in calculated ground-state deformations (see Fig. 7). The next region with the largest differences in the predictions is located between neutron numbers  $N = 236$  and 258 (see Fig. 12). However, these differences are not critical because (a) this region is not expected to play a role in the  $r$  process, (b) expected  $\alpha$ -decay half-lives exceed  $10^{20}$  s (see Fig. 13), and (c) many of the nuclei in this region are not expected to decay by  $\alpha$  emission. High  $\Delta Q_{\alpha}$  values [ $\Delta Q_{\alpha}(Z, N) \approx 1.5$  MeV] are observed near shell closure at  $N = 184$  and in very neutron-rich nuclei near the two-neutron drip line. This is a consequence of the difference in the predictions of the ground-state properties such as deformations in the nuclei near  $N = 184$  (see Ref. [59]) and general deterioration of predictive power of nuclear models on approaching the neutron drip line (see Ref. [39]). In other regions of the nuclear chart,  $\Delta Q_{\alpha}(Z, N) \leq 1.0$  MeV with smallest spreads seen in the  $N < 180$  nuclei.

Note that the inclusion of dynamical correlations (for example, by means of a five-dimensional collective Hamiltonian) can locally modify the binding energies and  $Q_{\alpha}$  values [63,68,86] but they have the largest impact on transitional nuclei which represent only a minor part of the nuclei under

<sup>8</sup>A similar increase is also seen in the vicinity of the  $N = 258$  shell closure in the calculations with the NL3\* and PC-PK1 CEDFs [see Figs. 11(c) and 11(d)].

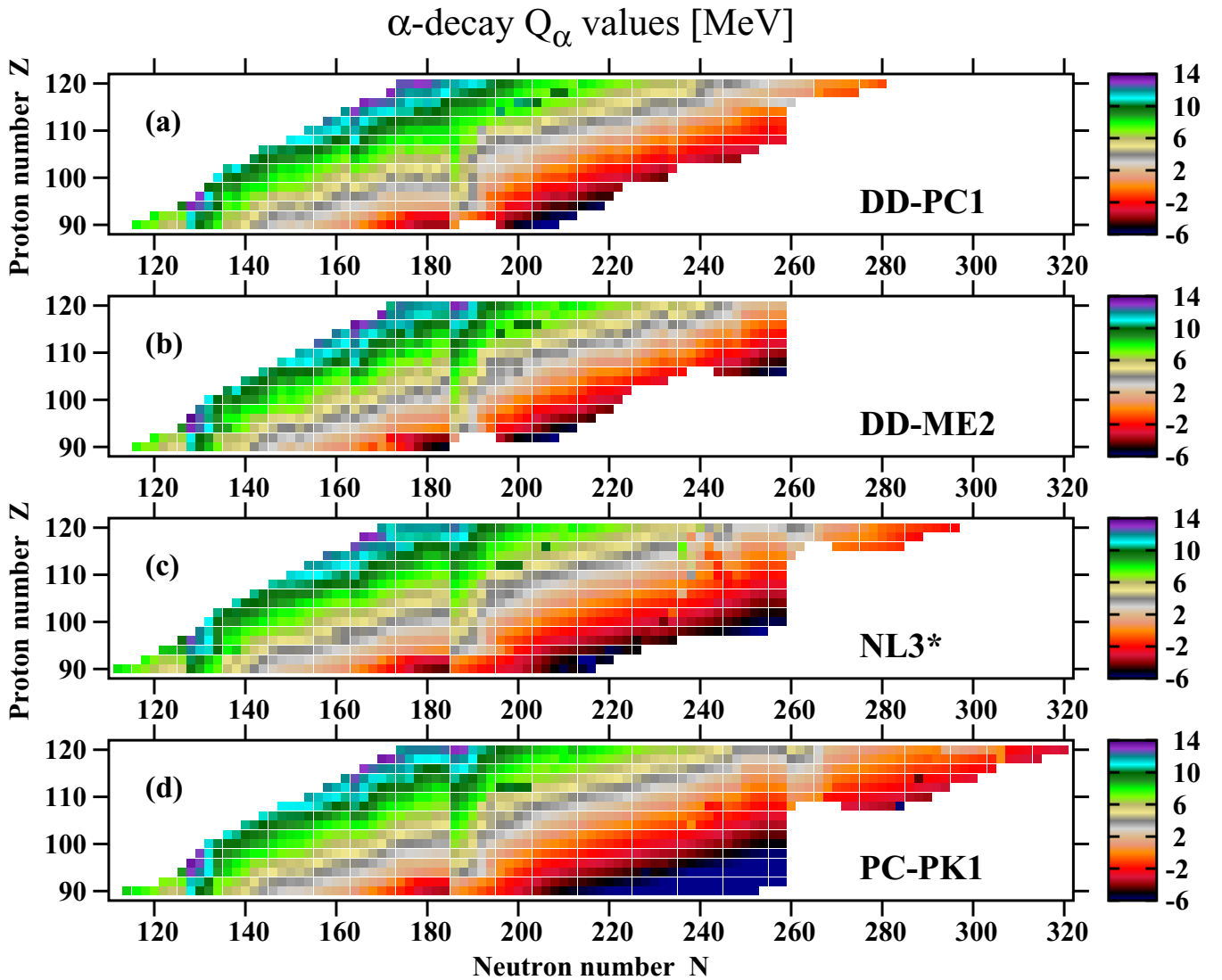


FIG. 11. The  $Q_\alpha$  values for even-even actinides and superheavy nuclei calculated with indicated CEDFs.

study. For well-deformed nuclei, the impact of dynamical correlations on  $Q_\alpha$  values is rather modest [63]. Thus, their inclusion is not expected to change drastically the global picture for the behavior of  $Q_\alpha$ .

Calculated  $\alpha$ -decay half-lives  $\tau_\alpha$  (in logarithmic scale) obtained with the VSS-2005 empirical formula for four CEDFs are shown in Fig. 13. Other phenomenological formulas such as VSS-1989, MB-2016, and Royer-2000 give similar results; thus, they are not shown. For a given isotope chain the cal-

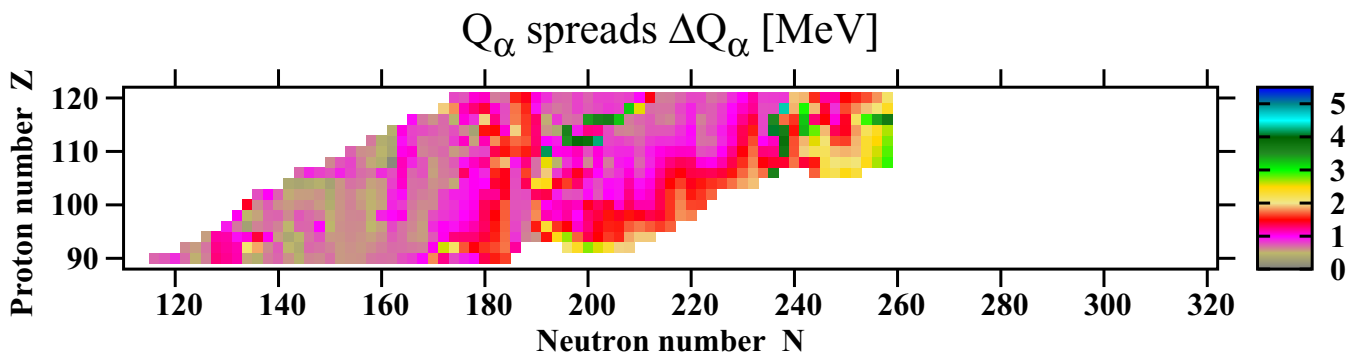


FIG. 12. The  $Q_\alpha$  spreads  $\Delta Q_\alpha(Z, N)$  as a function of proton and neutron number.  $\Delta Q_\alpha(Z, N) = |Q_\alpha^{\max}(Z, N) - Q_\alpha^{\min}(Z, N)|$ , where  $Q_\alpha^{\max}(Z, N)$  and  $Q_\alpha^{\min}(Z, N)$  are the largest and smallest  $Q_\alpha$  values obtained with four employed CEDFs for the  $(Z, N)$  nucleus.

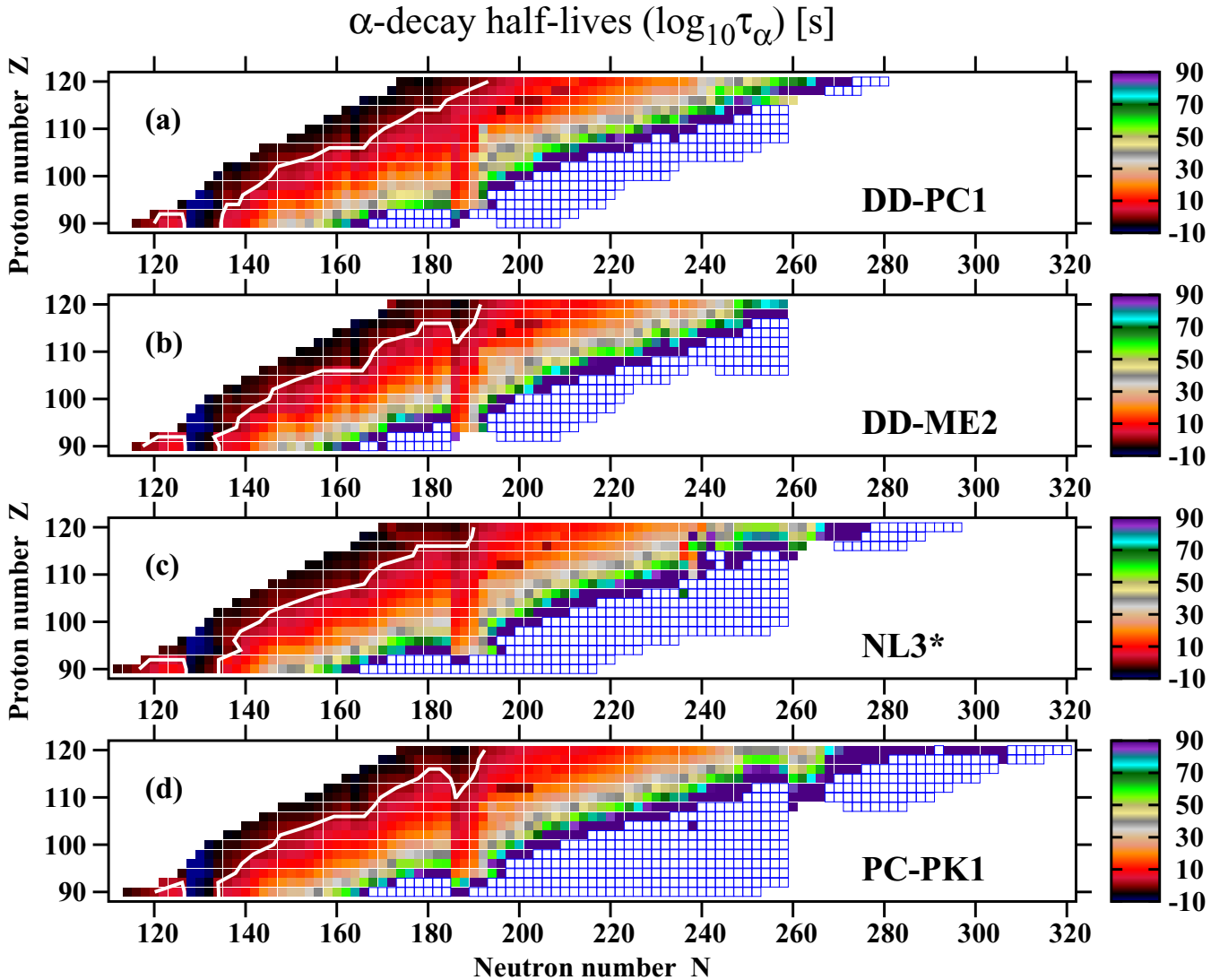


FIG. 13. Calculated  $\log_{10}(\tau_\alpha)$  values of the  $\alpha$  decays for even-even superheavy nuclei obtained with the VSS-2005 version of the Viola-Seaborg semiempirical formula for four indicated CEDFs. Open squares are used for the nuclei in which  $\alpha$  decay is energetically forbidden. The white line corresponding to  $\log_{10}(\tau_\alpha) = 1.0$  outlines the region of nuclei in which the alpha-decay half-life is smaller than 10 s.

culated half-lives generally increase with increasing neutron number. This trend is interrupted only at the  $N = 184$  and 258 shell closures. The consequence of this feature is the fact that the traditional experimental technique of detecting superheavy nuclei by  $\alpha$  decay will not work in neutron-rich nuclei because they can decay faster by spontaneous fission. Note that  $\alpha$  decay is energetically forbidden for a large group of very neutron-rich nuclei located in the vicinity of the neutron-drip line. In such nuclei as well as in those which have very large  $\tau_\alpha$  values, the competition of spontaneous fission, neutron induced fission,  $\beta$  decay, and neutron emission will define the leading channel of decay in the  $r$ -process calculations.

It is important to remember that the typical timescale of the  $r$  process is in the seconds range [2–4]. Figure 13 clearly illustrates that with few exceptions the nuclei located to the right of white lines have  $\alpha$ -decay half-lives exceeding 10 s. Thus,  $\alpha$ -decay half-lives of these nuclei are longer than the

typical timescale of the  $r$  process and, as a consequence, their  $\alpha$  decays will not affect the  $r$ -process simulations. These white lines in Fig. 13 also outline the region of the nuclear chart in which traditional experimental measurements of superheavy nuclei based on the  $\alpha$  decays are possible: these are the regions located near and to the left of these white lines.

Theoretical uncertainties in the predictions of  $\alpha$ -decay half-lives given via the  $\Delta[\log_{10}(\tau_\alpha)]$  spreads are summarized in Fig. 14. The comparison of panels (a) and (b) clearly shows that these uncertainties mostly emerge from the differences in the predictions of the  $Q_\alpha$  values by different functionals. These uncertainties exceed 50 orders of magnitude in the nuclei located in the vicinity of the two-neutron drip line and in some nuclei around  $Z \approx 108$ ,  $N \approx 198$  (see Fig. 14). The uncertainties in  $\tau_\alpha$  originating from different empirical formulas [see Eqs. (19)–(21)] are significantly smaller [see Fig. 14(b)]. For absolute majority of the nuclei they are



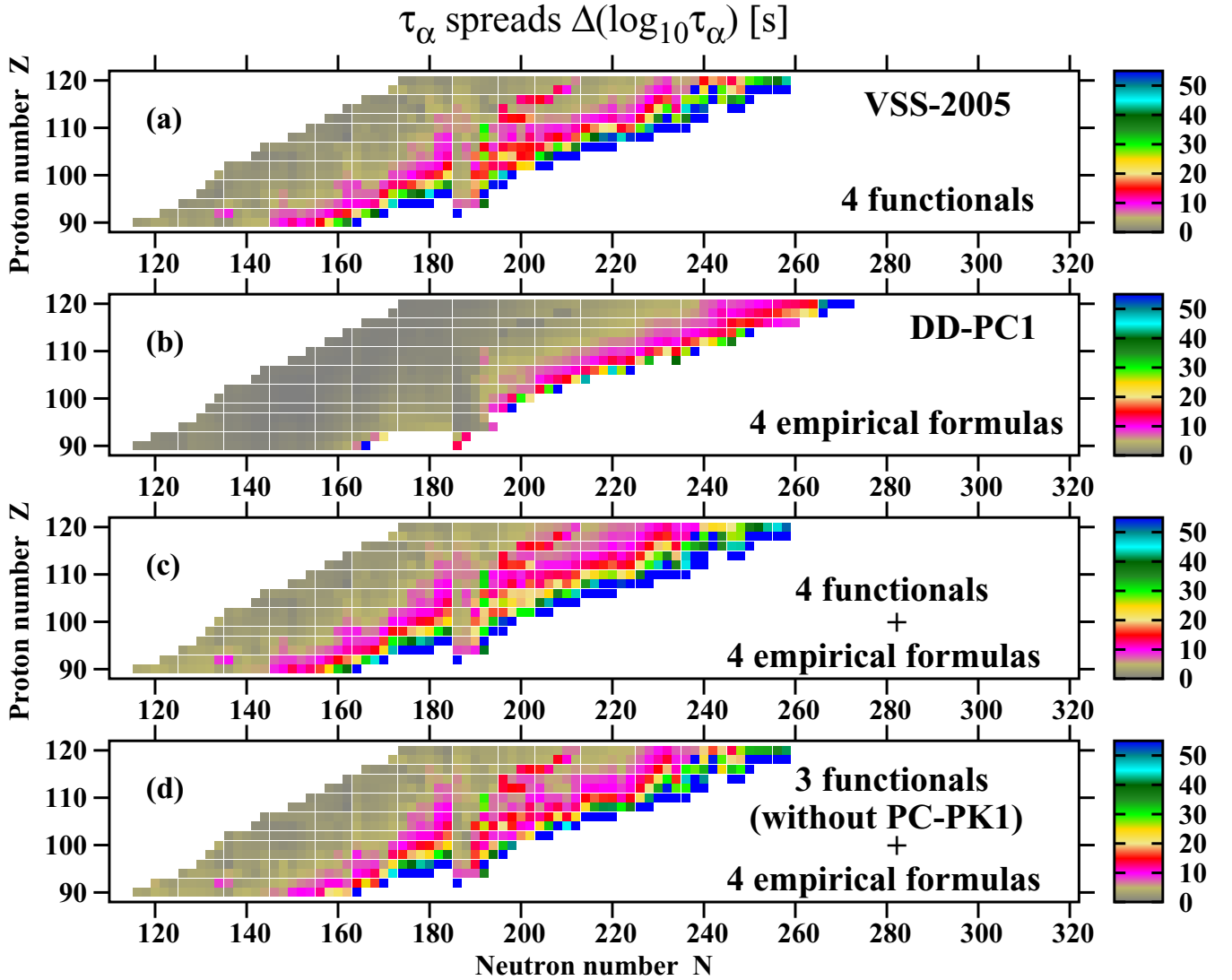


FIG. 14. The  $\tau_\alpha$  spreads  $\Delta\tau_\alpha(Z, N)$  as a function of proton and neutron number.  $\Delta\tau_\alpha(Z, N) = |\tau_\alpha^{\max}(Z, N) - \tau_\alpha^{\min}(Z, N)|$ , where  $\tau_\alpha^{\max}(Z, N)$  and  $\tau_\alpha^{\min}(Z, N)$  are the largest and smallest  $\tau_\alpha$  values obtained with a selected set of functionals and empirical formulas. Panel (a) shows these spreads obtained with four employed CEDFs and the VSS-2005 empirical formula. The DD-PC1 CEDF and four empirical formulas are used in panel (b). Panel (c) presents the combined spread of  $\tau_\alpha$  obtained with four CEDFs and four empirical formulas. Panel (d) is the subversion of panel (c) in which the PC-PK1 functional is excluded.

smaller than five orders of magnitude and for proton-rich nuclei and the nuclei located close to the  $\beta$  stability they are very small. They are larger than ten orders of magnitude only in neutron-rich nuclei located in close vicinity of the two-neutron drip line. Combined theoretical uncertainties in  $\tau_\alpha$  emerging from the use of four empirical formulas and four CEDFs are summarized in Fig. 14(c). One can see that for almost half of nuclei they exceed ten orders of magnitude; these nuclei are located on the neutron-rich side of the nuclear chart. However, these uncertainties are not very critical since the  $\alpha$ -decay lifetimes become extremely large in such nuclei (see Fig. 13) so  $\alpha$  decay can compete neither with fission nor with  $\beta$  decay. Note also that the removing of the PC-PK1 functional from consideration does not change appreciably theoretical uncertainties in the predictions of  $\alpha$ -decay half-lives [compare Figs. 14(c) and 14(d)].

## V. FISSION PROPERTIES

### A. Primary fission barriers

The distributions of primary fission barrier<sup>9</sup> heights in the  $(Z, N)$  plane obtained with employed functionals are shown in Fig. 15. Figure 16 presents the maps of the nuclei in the region under study in which outer fission barriers are higher than inner ones in the RS-RHB calculations (see Figs. 2 and 3 for more details). It also illustrates that the importance of outer fission barriers in stabilization of nuclei in general decreases on going from light actinides to superheavy nuclei because

<sup>9</sup>The highest in energy fission barrier (among inner and outer ones) is called primary and it plays an important role in the  $r$ -process modeling (see Ref. [85]).

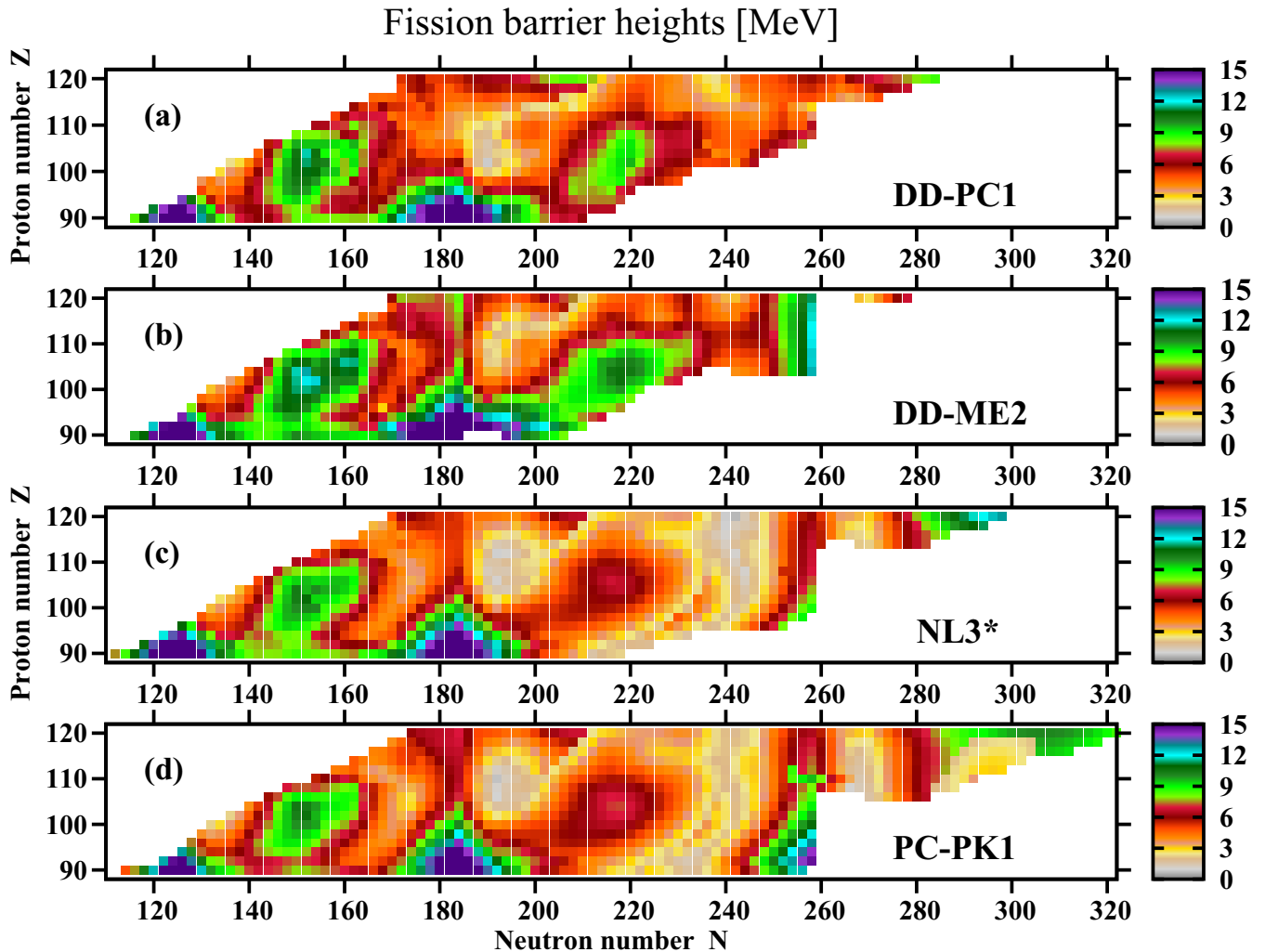


FIG. 15. The heights of primary fission barriers (in MeV) obtained in axial RS-RHB and RA-RHB calculations as a function of proton and neutron numbers for nuclei located between two-proton and two-neutron drip lines.

of increased importance of Coulomb interaction (compare Figs. 3 and 2). Figure 16 also demonstrates the impact of octupole deformation (as obtained in RA-RHB calculations) on the outer fission barriers and on their heights with respect to inner ones. The lowering of the outer fission barrier due to octupole deformation indicates that asymmetric fission becomes dominant, while the absence of the impact of octupole deformation on outer fission barrier height indicates that fission will be symmetric.

Figure 16 shows that similar regions in the  $(Z, N)$  plane, in which the outer fission barriers are higher in energy than inner ones in the RS-RHB calculations, appear in the calculations with all employed functionals. However, these regions are substantially larger in the density dependent functionals (such as DD-PC1 and DD-ME2) as compared with CEDFs NL3\* and PC-PK1. Octupole deformation does not affect outer fission barriers in the nuclei located in the  $Z \sim 110, N \sim 240$  region, in the  $N \leq 120$  nuclei, or in the nuclei located not so far away from  $N \approx 180$ . On going away from the latter two regions, octupole deformation starts to reduce the heights of outer fission barriers but they still remain higher in energy

than inner ones. Further transition away from these regions leads to the reduction of the heights of outer fission barriers below the inner ones due to the impact of octupole deformation.

Figure 15 reveals a lot of similarities in the predictions of the global structure of the maps of fission barrier heights obtained with employed functionals. The highest PFBs are predicted in the islands of low- $Z$  nuclei centered around spherical shell closures with  $N = 126$  and  $184$  (and  $N = 258$  in the case of the PC-PK1 functional). Fission barriers reach 15 MeV in the centers of these islands. The next island with high fission barriers exists around  $Z \approx 100, N \approx 150$ . The left bottom part of this island coincides with the region of actinides (see, for example, Fig. 7 in Ref. [62]) in which the heights of fission barriers have been experimentally measured. Relativistic mean-field calculations with the NL3\*, PC-PK1, and DD-PC1 functionals performed by different groups rather well describe inner and outer fission barriers in actinides [62–64,69]. Note also that the spreads of the heights of inner fission barriers obtained with these three functionals in the  $Z \approx 100, N \approx 150$  island are relatively small

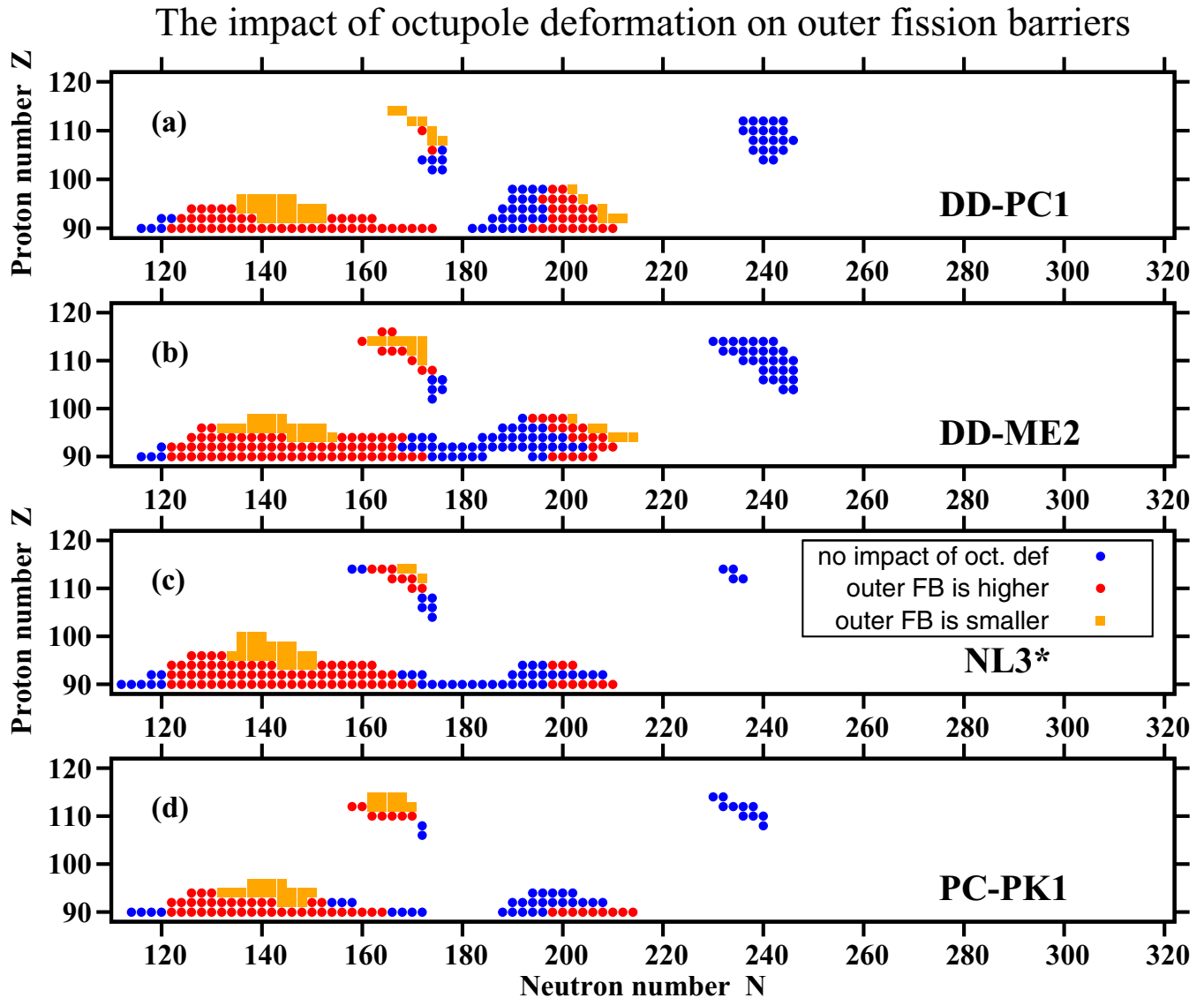


FIG. 16. The distributions of the nuclei, in which the outer fission barrier is higher than the inner one in the RS-RHB calculations, in the  $(Z, N)$  plane for four employed CEDFs. Different types of symbols are used to indicate the impact of octupole deformation on outer fission barriers of these nuclei. Blue solid circles are used for the nuclei, the heights of the outer fission barriers of which are not affected by the inclusion of octupole deformation. Solid red circles/orange squares are used for the nuclei in which the outer fission barrier is affected by octupole deformation in the RA-RHB calculations and is higher/lower than the inner fission barrier.

(approximately 1 MeV or less) for the majority of nuclei in this island [see Fig. 3(b) in Ref. [47]]. In contrast, the DD-ME2 functional predicts somewhat higher fission barriers in this island [see Fig. 15(b)] which leads to somewhat higher spreads  $\Delta E^B$  in the heights of primary fission barriers [see Fig. 17(a)]. The island of low fission barriers is seen near  $Z \approx 108, N \approx 192$  in all functionals. Then another island of high fission barriers centered around  $Z \approx 104, N \approx 216$  is formed. The highest fission barriers reaching 10–11 MeV in the center of this island are predicted by the DD-ME2 functional [see Fig. 15(b)]. Somewhat lower fission barriers (with approximately 9 MeV height in the center of the island) are predicted by the DD-PC1 functional [see Fig. 15(a)]. Fission barriers with height of approximately 6 MeV appear in a broad region of this island in the calcu-

lations with the NL3\* and PC-PK1 CEDFs [see Figs. 15(c) and 15(d)].

With increasing neutron number the predictions start to differ substantially. The NL3\* and PC-PK1 functionals predict extremely low fission barriers with heights of around 2 MeV or less for the band of nuclei around  $N \approx 240$  [see Figs. 15(c) and 15(d)]. No such band is formed in the calculations with DD-ME2 and DD-PC1 functionals [see Figs. 15(a) and 15(b)]. This could have a drastic impact on the creation of superheavy elements in the  $r$  process because the nuclear flow during most of the neutron irradiation step of the  $r$  process follows the neutron drip line and produces in tens of ms the heaviest drip line nuclei (see the discussion in Sec. 4 of Ref. [12]). However, this nuclear flow will most likely be terminated at  $N \approx 240$  nuclei in the calculations with NL3\* and PC-PK1

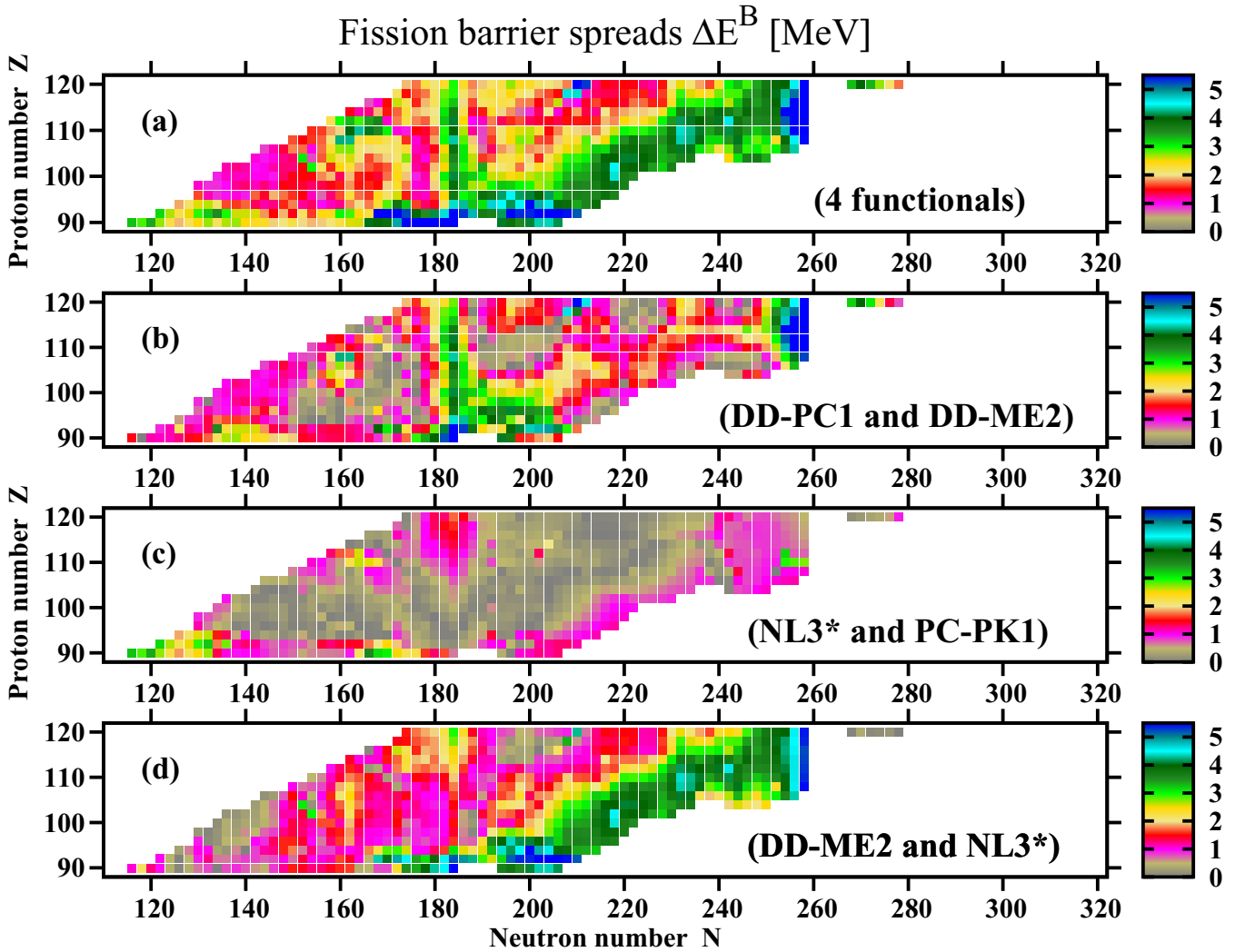


FIG. 17. (a) The spreads  $\Delta E^B$  of the heights of primary fission barriers as a function of proton and neutron numbers.  $\Delta E^B(Z, N) = |E_{\max}^B(Z, N) - E_{\min}^B(Z, N)|$ , where, for given  $Z$  and  $N$  values,  $E_{\max}^B(Z, N)$  and  $E_{\min}^B(Z, N)$  are the largest and smallest heights of inner fission barriers obtained with the employed set of four functionals. (b)–(d) The spreads  $\Delta E^B$  obtained for indicated pairs of the functionals.

since fission will be much faster than neutron capture. Thus, no superheavy nuclei are expected to be formed beyond  $N \sim 240$  in the  $r$ -process calculations based on fission barriers obtained with these two functionals. This is similar to the results of the  $r$ -process simulations based on nonrelativistic models (such as the Skyrme DFT with HFB-14 functional, Thomas-Fermi model, and finite range droplet model) with low fission barriers in the vicinity of the neutron drip line [12,15]. In contrast, the formation of superheavy elements with  $N > 240$  in the  $r$  process is more likely in the calculations based on the DD-ME2 and DD-PC1 functionals since the  $(Z, N)$  region near the neutron drip line is characterized by relatively high fission barriers [see Figs. 15(a) and 15(b)]. As a consequence, neutron capture is expected to proceed faster than fission and nuclear flow during the neutron irradiation step of the  $r$ -process could extend to higher proton numbers [12,15]. To a degree this is similar to the  $r$ -process simulations based on the models (such as the extended Thomas-Fermi

model) with high fission barriers near the neutron drip line (see Ref. [15]).

Further increase of neutron number leads to a rise of the heights of primary fission barriers and the formation of the band of nuclei near shell closure at  $N = 258$  with the heights of PFBs exceeding 6 MeV [see Figs. 15(b)–15(d)]. In some nuclei they even reach 12–15 MeV in the calculations with PC-PK1 and NL3\* CEDFs [see Figs. 15(c) and 15(d)]. Note that this process is suppressed in the calculations with CEDF DD-PC1 [see Fig. 15(a)] because of reduced impact of the  $N = 258$  spherical shell gap on the ground-state deformations [see Fig. 5(a)]. The nuclear landscape extends substantially beyond  $N = 258$  in the calculations with NL3\* and PC-PK1 [see Figs. 15(c) and 15(d)]. In this region we again see the alteration of the regions of low (near  $N \approx 268$ ) and high (near  $N \approx 280$  and above) PFBs. Note that in the  $N > 258$  region toroidal shapes [65,100] could become the lowest in energy solutions. This has been verified in the calculations with the



DD-PC1 functional in Ref. [66] but has not been checked for other functionals.

### B. Theoretical uncertainties in primary fission barriers and their sources

The spreads  $\Delta E^B$  of the heights of primary fission barriers as a function of proton and neutron numbers for four employed functionals are shown in Fig. 17(a). One can see that on the average they are moderate (on the level of 1.0–1.5 MeV) in the neutron-poor region of actinides centered around ( $Z \sim 100, N \sim 140$ ). Then the spreads start to increase with a small island of high  $\Delta E^B \approx 4.0$  MeV values seen in superheavy nuclei around  $Z \approx 110, N \approx 164$ . Further increase of neutron number leads to the band of high  $\Delta E^B \approx 4.0$  MeV values for the nuclei with  $N \approx 184$ . The sources of these uncertainties are directly related to the differences in the predictions of the ground-state properties of these nuclei: spherical ground states are predicted in these nuclei in the calculations with PCPK1, DD-ME2, and NL3\* functionals [see Figs. 5(b)–5(d)] while the DD-PC1 functional prefers oblate ground states in superheavy  $N \approx 184$  nuclei [see Fig. 5(a)]. After crossing this band, theoretical uncertainties in the heights of primary fission barriers substantially decrease and for the majority of the nuclei located inside the triangle with the sides  $N = 188$  (for  $Z = 96$ –120),  $Z = 120$  (for  $N = 188$ –240), and ( $Z = 96, N = 188$  to  $Z = 120, N = 240$ ) they are in general better than 2.5 MeV and in many nuclei they are even better than 1.5 MeV. However, the  $\Delta E^B$  spreads start to increase again on approaching the two-neutron drip line. Here they form a quite wide band of the nuclei parallel to the two-neutron drip line in which  $\Delta E^B$  is close to 4.0 MeV. Even higher spreads reaching 5.5 MeV are seen near shell closure at  $N = 258$ .

The analysis of the spreads  $\Delta E^B$  allows us to identify major sources of theoretical uncertainties in the predictions of the heights of PFBs. These could be reduced to two major contributors, namely, underlying single-particle structure mostly affecting the ground-state properties and nuclear matter properties of employed CEDFs. To facilitate the discussion we will consider the  $\Delta E^B$  spreads for the pairs of selected functionals.

The lowest spreads exist for the pair of the NL3\* and PC-PK1 functionals [see Fig. 17(c)]:  $\Delta E^B \leq 0.5$  MeV for the absolute majority of the nuclei and only in specific regions of the nuclear chart it is higher. Even in those regions it is higher than 1 MeV only for a limited set of the nuclei. These regions are (i) the actinides around  $N = 126$ , (ii) the  $Z = 90$  and 92 actinides with  $N \approx 170$ , (iii) superheavy nuclei in the vicinity of the  $Z = 120$  and  $N = 184$  lines, (iv) very neutron-rich nuclei in the vicinity of the two-neutron drip line, and (v) the band of the nuclei around  $N \approx 246$ . The differences in the predictions of the heights of outer fission barriers are responsible for the spreads in the region (i). At present, their source is not clear. The spreads  $\Delta E^B$  seen in the region (ii) are due both to different proton and neutron dependencies of the impact of octupole deformation on outer fission barriers in the NL3\* and PC-PK1 functionals [compare panels (c) and (d) of Fig. 16] and to the fact that in some nuclei we compare the heights of outer and inner fission barriers. In the

region (iii), the large  $\Delta E^B$  values are due to the differences in the predictions of the spherical shell closures at  $Z = 120$  and  $N = 184$  and the densities of the single-particle states in their vicinities (see Fig. 1 in Ref. [59] and the discussion in this reference). Slightly different isovector properties of the NL3\* and PC-PK1 functionals (see Table II) may be responsible for the divergence of their predictions in the region (iv). The large  $\Delta E^B$  values in the region (v) are due to prolate-oblate-spherical shape coexistence which takes place in slightly different regions of the ( $Z, N$ ) chart in these two functionals [compare Figs. 5(c) and 5(d)].

The comparison of the predictions of the NL3\* and PC-PK1 functionals for the fission barriers is quite illuminating since it shows in a global way a number of important features. First, apart from the regions (i)–(v) the comparable (typically within 0.5 MeV) predictions for the heights of PFBs are obtained on a global scale by these two functionals despite the fact that they differ substantially in the predictions of the ground-state energies in neutron-rich nuclei (see the discussion of Fig. 8). Thus, the description of the ground-state energies is to a degree decoupled from the description of fission barriers; the latter depends on the relative energies of the saddle and the ground state. As a consequence, good description of the ground-state energies does not guarantee good description of the fission barriers and vice versa. Second, the differences in the predictions of the PFB heights seen in the regions (iii) and (v) are related to the differences in the predictions of the ground-state properties, which in turn are defined by the differences in the underlying single-particle structure. Third, if we exclude the regions (i)–(v) from consideration it becomes clear that some differences in nuclear matter properties such as the symmetry energy  $J$  and its slope  $L_0$  (see Table II) do not lead to important differences in the predictions for PFBs. Fourth, comparable global predictions for the PFBs are obtained despite underlying differences in the basic structure of the functionals and their fitting protocols. The NL3\* functional includes meson exchange of finite range, while the PC-PK1 CEDF does not have mesons and thus it has zero range interactions (see Ref. [58]). The fitting protocol of the CEDF NL3\* is based on 12 spherical nuclei and includes empirical data on nuclear matter properties (see Ref. [43]), while the one for PC-PK1 includes only data on binding energies (60 spherical nuclei) and charge radii (17 spherical nuclei) [50]. Note that the NL3\* and PC-PK1 functionals have six and nine parameters, respectively. However, the analysis of parametric correlations shows that in reality there are only five and six independent parameters in these two functionals [46,58].

Next we consider the spreads  $\Delta E^B$  obtained with the NL3\*/DD-ME2 pair of the functionals [see Fig. 17(d)]. These two functionals have almost identical fitting protocols (see Refs. [42,43]). The only difference is the fact that the DD-ME2 fitting protocol uses three experimental data points on neutron skins as compared with four in NL3\* but the impact of this difference is expected to be small. Thus, larger values of the  $\Delta E^B$  spreads in the NL3\*/DD-ME2 pair as compared with the ones in the NL3\*/PC-PK1 pair are related to the basic difference of these two functionals, namely, to the implementation of density dependence. The DD-ME2 functional

has explicit dependence of the meson-nucleon coupling on the nucleonic density, while NL3\* employs cubic and quartic powers of the  $\sigma$  meson for density dependence (see Sec. II of Ref. [39] for details). In addition, the nuclear matter properties (in particular, the symmetry energy  $J$  and its slope  $L_0$ ) of these two functionals differ substantially (see Table II) and this difference is expected to contribute to the increase of the spreads  $\Delta E^B$  obtained for the NL3\*/DD-ME2 pair as compared with those for the NL3\*/PC-PK1 pair.

Finally, the  $\Delta E^B$  spreads for the DD-PC1/DD-ME2 pair of the functionals are presented in Fig. 17(b). Nuclear matter properties of these two functionals are close to each other and they are located within the limits of the SET2b constraint set on the experimental/empirical ranges for the quantities of interest derived in Ref. [51] (see Table II). However, fitting protocols of these two functionals are drastically different: CEDF DD-ME2 is fitted to the properties of 12 spherical nuclei (see Ref. [43]) while DD-PC1 is defined by the properties of 64 deformed rare-earth nuclei and actinides (see Ref. [44]). As a result of this difference in fitting protocols, the largest  $\Delta E^B$  spreads appear in the vicinity of spherical shell closures at  $N = 184$  (with  $\Delta E^B$  reaching 4.0 MeV) and  $N = 258$  (with  $\Delta E^B$  reaching 5.5 MeV) [see Fig. 17(b)]. Indeed, the impact of these shell closures on the equilibrium deformation differs substantially in these two functionals [compare Figs. 5(a) and 5(b) and see Fig. 7(b)] and this is a reason for increased  $\Delta E^B$  spreads.

### C. Comparison with the results obtained in nonrelativistic calculations

It is interesting to compare the global trends of the heights of PFB in the  $(Z, N)$  plane obtained in the RHB calculations (see Fig. 15) with those obtained in earlier nonrelativistic calculations for which maps similar to those presented in Fig. 15 are available. Note that similar to our calculations all these nonrelativistic calculations have been performed only for axial nuclear shapes.

Fission barriers obtained in Gogny DFT calculations with the D1M\* functional are presented in Fig. 12 of Ref. [23]. These calculations cover the region from the two-proton drip line up to the nuclei with two-neutron separation energies of  $S_{2n} = 4.0$  MeV. In these calculations, the fission barriers of the  $N \leq 186$  nuclei typically exceed 6 MeV and in a number of these nuclei their heights are close to 12 MeV. Then fission barriers in the  $N \approx 190$ –210 nuclei are lower than 4 MeV but they increase to approximately 8 MeV on approaching the  $S_{2n} = 4.0$  MeV line. The differences in the predictions of the heights of PFB obtained in the CDFT and Gogny DFT calculations (compare Fig. 15 with Fig. 12 of Ref. [23]) are in part related to the differences in the predictions of ground-state properties (compare Fig. 5 in the present paper with Fig. 5 in Ref. [23]).

Our results for fission barriers (Fig. 15) could also be compared with those obtained in nonrelativistic DFTs with the BCPM and HFB14 functionals and FRLDM (see Fig. 7 in Ref. [18]). The calculations with HFB14 predict very low fission barriers (with  $E^B < 4$  MeV) for the  $Z \geq 110$  nuclei with exceptionally low fission barriers ( $E^B < 2$  MeV) in many

nuclei located in the  $N \approx 184$ –210 region (see middle panel of Fig. 7 in Ref. [18] and Fig. 13 in Ref. [85]). The RHB calculations predict in general higher fission barriers (as compared with HFB14 ones), but a similar island of low fission barriers is seen near  $Z \approx 108$ ,  $N \approx 192$  in all functionals (see Fig. 15). However, this island is narrower as compared with the HFB14 one. Fission barriers obtained with the BCPM functional and FRLDM are somewhat higher than those obtained with HFB14 (compare top and bottom panel with middle panel of Fig. 7 in Ref. [18]). However, they share the same general structure in the  $(Z, N)$  plane.

Fission barriers calculated in the DFT framework with Skyrme SLy6, SkI3, SV-min, and SV-bas functionals are presented in Fig. 5 of Ref. [21]. Unfortunately, the color map used in this figure does not allow us to extract the details in the most interesting energy range of 6–10 MeV.<sup>10</sup> However, the region of low fission barriers (with  $E^B < 4$  MeV) similar to that discussed above appears in all functionals for  $N \approx 190$ –210,  $Z \approx 94$ –120. Fission barriers obtained in the TF and ETFSI models for the  $(Z = 84$ –120,  $N = 140$ –236) and  $(Z = 84$ –115,  $N = 140$ –216) regions of the nuclear chart are presented in Fig. 2 of Ref. [15]. Both of these models show the island of low fission barriers centered around  $Z \approx 110$ ,  $N \approx 192$ . In general, the ETFSI results are close to the above-mentioned results obtained with Skyrme EDFs.

## VI. CONCLUSIONS

A systematic investigation of the ground-state and fission properties of even-even actinides and superheavy nuclei with  $Z = 90$ –120 from the two-proton up to two-neutron drip lines has been performed for the first time in the framework of covariant density-functional theory. Four state-of-the-art CEDFs such as DD-PC1, DD-ME2, NL3\*, and PC-PK1 are used in this paper. They represent the major classes of the CDFT models which differ by basic assumptions and fitting protocols. This allows a proper assessment of systematic theoretical uncertainties for physical observables of interest. Obtained results provide a necessary theoretical input for the  $r$ -process modeling in heavy nuclei and, in particular, for the study of fission cycling. The main results can be summarized as follows.

- (1) Quadrupole deformations of calculated ground states and related theoretical uncertainties have been investigated. It turns out that four employed functionals predict very similar deformations for the majority of the nuclei. However, large theoretical uncertainties in quadrupole deformation exist for some nuclei but they are well localized in the  $(Z, N)$  plane. These uncertainties are mostly due to the uncertainties in the predictions of the underlying single-particle structure. They are dominated by the uncertainties in the predictions of both spherical shell closures at  $N = 184$ ,  $N =$

<sup>10</sup>A better color map for the fission barrier height distribution in the  $(Z, N)$  plane obtained with the Skyrme SV-min functional is used in Fig. 4 of Ref. [22].

258, and  $Z = 120$  (for the  $N < 190$  nuclei) and deformed single-particle structures leading to somewhat different boundaries in the  $(Z, N)$  plane between the regions with oblate and prolate shapes. The differences in nuclear matter properties of employed functionals have only marginal impact on theoretical uncertainties related to calculated quadrupole deformations.

- (2) Theoretical uncertainties  $\Delta E(Z, N)$  in binding energies, emerging from poorly defined isovector properties of CEDFs, increase drastically when approaching the neutron drip line and in some nuclei they reach 50 MeV. However, they reduce substantially [down to a maximum value of  $\Delta E(Z, N) \approx 21$  MeV] when the PC-PK1 functional is removed from consideration. The two-neutron drip line of this functional is also located at substantially higher neutron numbers as compared with the ones obtained with other functionals. In addition, this functional is the major source of theoretical uncertainties in two-neutron separation energies. Parametric correlation leading to an overparametrization of the isoscalar channel is a possible reason for such a unique behavior of the CEDF PC-PK1. Theoretical uncertainties in two-neutron separation energies reveal a clear importance of the uncertainties in the  $N = 184$  and 258 spherical shell closures and in the location of the boundaries between the regions of prolate and oblate shapes.
- (3)  $\alpha$ -decay properties, such as the  $Q_\alpha$  values and the lifetimes  $\tau_\alpha$ , and related theoretical uncertainties have been investigated employing four empirical formulas and four CEDFs. While the predictive power of the models is relatively high on the proton-rich side of the nuclear chart, it starts to deteriorate on approaching  $N = 184$ . It is especially low in the nuclei around  $Z \approx 108, N \approx 198$  (the region of the transition from prolate to oblate ground states) and in very neutron-rich nuclei located in the vicinity of the two-proton drip line. However, the uncertainties in the latter region are not very important since the  $\alpha$  decay in these nuclei is not expected to play any role in the  $r$  process because of extremely large lifetimes.
- (4) The distributions of the primary fission barriers in the  $(Z, N)$  plane have been investigated with four employed CEDFs. Globally, the highest fission barriers are produced by the CEDF DD-ME2, and the lowest ones are produced by the NL3\* and PC-PK1 functionals. The results obtained with DD-PC1 are located between these two extremes but closer to the DD-ME2 ones. The presence of the band of nuclei with  $N \approx 240$  in the  $(Z, N)$  plane with low fission barriers, obtained in the calculations with the NL3\* and PC-PK1 functionals, could have a drastic impact on the creation of superheavy elements beyond  $N \sim 240$  in the  $r$  process. The nuclear flow during most of the neutron irradiation step of the  $r$  process follows the neutron drip line and produces in tens of ms the heaviest drip line nuclei. However, this nuclear flow will most likely be terminated at  $N \approx 240$  nuclei since fission will be much faster than neutron capture. In contrast, the formation

of superheavy elements with  $N > 240$  in the  $r$  process is more likely in the calculations based on the DD-ME2 and DD-PC1 functionals since the  $(Z, N)$  region near the neutron drip line is characterized by relatively high fission barriers and the band of nuclei with low fission barriers (similar to the one at  $N \approx 240$  in the NL3\* and PC-PK1 functionals) is absent.

- (5) There are two major sources of theoretical uncertainties in the predictions of the heights of PFBs, namely, underlying single-particle structure mostly affecting the ground-state properties and nuclear matter properties of employed CEDFs. For example, the increase of theoretical uncertainties for the ground states of the nuclei in the vicinity of the  $N = 184$  and 258 spherical shell closures leads to an increase of theoretical uncertainties for their fission barriers. The functionals with nuclear matter properties located in the vicinity of empirical SET2b estimates [51] tend to produce higher fission barriers as compared with the predictions of the functionals the nuclear matter properties of which are located outside the limits of the SET2b constraint set. The problem of finding the best functional for the description of fission barriers is further complicated by the fact that the description of the ground-state energies is to a degree decoupled from the description of fission barriers; the latter depends on the relative energies of the saddle and the ground state. As a consequence, good description of the ground-state energies does not guarantee good description of the fission barriers and vice versa.

This is the first ever systematic attempt within the covariant density-functional theory to provide both the input for the  $r$ -process calculations which includes the ground state and fission properties of actinides and superheavy nuclei and the assessment of systematic theoretical uncertainties in the physical quantities of interest. As such it follows the ideology of all previous nonrelativistic calculations of relevance for the  $r$  process of heavy and superheavy nuclei, which depend also on the fission processes, and assumes the axial symmetry of nuclei. This is a reasonable approximation for the ground-state properties of the majority of nuclei; the only exception is transitional nuclei which are soft in  $\gamma$  deformation. However, the restriction to axial symmetry leads to the fact that the calculated inner and outer fission barriers represent the upper limits and can be potentially lowered when the triaxiality is taken into account. The  $r$ -process simulations with the data obtained in this paper will allow us to limit the region of the  $(Z, N)$  plane which has an impact on this process. The hope is that, for this limited set of nuclei, systematic refined calculations taking into account the dynamical correlations and the triaxiality in the calculations of the part of the  $(\beta_2, \gamma)$ -plane covering ground state, inner fission barrier, and second minimum as well as triaxiality and octupole deformation in the calculations of the part of the  $(\beta_2, \beta_3, \gamma)$ -plane covering second minimum, outer fission barrier, and region beyond that will be possible in the era of exascale computing.

The underlying single-particle structure and nuclear matter properties of CEDFs emerge as the major sources of



theoretical uncertainties. However, they affect different physical observables in a different way. For example, theoretical uncertainties in the ground-state quadrupole deformations are defined mostly by the uncertainties in the underlying single-particle structure. In contrast, both factors contribute to theoretical uncertainties for fission barriers. The existence of appreciable theoretical uncertainties in the ground-state and fission properties calls for better covariant energy density functionals. The reduction of parametric correlations between the parameters of CEDFs is one possible way in that direction [55,58]. In addition, experimental studies of superheavy elements in the vicinity of the  $Z = 120$  and  $N = 184$  lines, planned at new facilities such as SHE factory [101], will hopefully provide critical data which will allow us to discriminate the predictions of different models. Such information could be used for a better constraint of the CEDFs and thus for the reduction of substantial theoretical uncertainties in this region of the nuclear chart which affect all physical observables of interest and have a direct impact on the modeling of the  $r$  process.

#### ACKNOWLEDGMENTS

This material is based upon work supported by the US Department of Energy, National Nuclear Security Administration under Grant No. DE-NA0002925; by the US Department of Energy, Office of Science, Office of Nuclear Physics under Grant No. DE-SC0013037; and by Ghana Atomic Energy Commission, National Nuclear Research Institute, Ghana.

#### APPENDIX A: NEGLECT OF DYNAMICAL CORRELATIONS IN THE FISSION BARRIER CALCULATIONS

Some nonrelativistic calculations, mentioned in the last paragraph of Sec. II, take into account dynamical correlations, but others do not. Dynamical correlations are not taken into account in our calculations due to the following reasons.

First, the analysis performed in Ref. [86] in the CDFT-based approach indicates that in most of the nuclei dynamical correlations modify fission barrier heights by less than 1 MeV but increase substantially computational time. The only exceptions are the nuclei with soft potential-energy surfaces the ground-state energy minimum of which is located at spherical shape. Note that the absolute majority of the nuclei under consideration are deformed in the ground states (see Sec. III). Thus, the errors introduced into the fission barrier heights due to neglect of dynamical correlations are expected to be smaller than the ones which are coming from the selection of CEDFs (see Sec. VB). In addition, theoretical uncertainties in fission barrier heights defined by their spreads [see Eq. (1)] are not expected to be modified much by the neglect of dynamical correlations. This is because in the majority of the cases the topology of the potential-energy surface of a given nucleus weakly depends on the underlying functional (see, for example, Figs. 7 and 8 in Ref. [47], Fig. 8 in Ref. [78], and supplemental material to Ref. [86]). As a consequence, dynamical correlations are expected to be comparable for

different functionals and they will at least partially cancel each other in Eq. (1).

Second, the inner fission barriers are lowered when the triaxiality is taken into account (see Ref. [62] and references quoted therein) and the potential-energy surfaces of the ground states in many superheavy nuclei are soft in  $\gamma$  deformation (see Ref. [102] and Appendix B.) In the CDFT calculations, the outer fission barriers can also be affected by triaxial deformation<sup>11</sup> via two mechanisms. In the first one, the saddle of the reflection-symmetric triaxial fission path becomes lower in energy than the saddle of the reflection-asymmetric (octupole-deformed) axial fission path due to underlying shell structure [78]. In the second mechanism, the reflection-symmetric fission path and its saddle lose their axial symmetry and attain some degree of triaxiality [64,69]. The investigations of the impact of dynamical correlations on fission barriers in triaxial calculations are very rare and quite limited in coverage. In nonrelativistic frameworks, only a limited set of actinides [104–107] and superheavy [108] nuclei has been studied so far. The impact of dynamical correlations on fission barriers of a restricted set of superheavy nuclei along the  $Z = 120$  isotopic and  $N = 174$  and 184 isotonic chains has been studied in the CDFT-based framework in Ref. [86].

Third, dynamical calculations do not provide a unique answer because of underlying assumptions and approximations [18,23,36,104,106,109,110]. For example, there exist substantial differences between the predictions based on Adiabatic Time Dependent HFB (ATDHFB) and Generator Coordinate Method (GCM) [based on Gaussian overlap approximation (GOA)] schemes [18,23,36,109]. The differences between spontaneous fission half-lives  $\tau_{SF}$  obtained in these two schemes could reach many orders of magnitude and increase with the decrease of the fissility-related parameter  $Z^2/A$  (which is equivalent to the increase of neutron number within a given isotopic chain; see Fig. 2 in Ref. [23]). Large differences between experimental and calculated  $\tau_{SF}$  also exist; for example, in the U isotopes these differences reach almost 20 orders of magnitudes when ATDHFB values for  $\tau_{SF}$  are used [23]. As illustrated in Refs. [104,106] on the example of the  $^{250,264}\text{Fm}$  and  $^{240}\text{Pu}$  nuclei, the inclusion of pairing fluctuations within a least-action approach improves the agreement between the predicted  $\tau_{SF}$  values and experiment. However, it remains to be seen whether that is a general conclusion applicable to all nuclei. In addition, such calculations are prohibitively expensive (in part, because of breaking of axial symmetry) and thus are not scalable to global calculations.

In addition, the treatment of the ground-state energy  $E_0$  (which is also tunneling energy for fission) relies on simplified approximations in the majority of the publications (see discussion in Ref. [86]). In microscopic calculations, tunneling energy is associated with the energy of the collective ground state defined either in GCM [111] or in the five-dimensional

<sup>11</sup>The important role of triaxiality in the description of outer fission barriers of actinides has also been discussed in the framework of the microscopic plus macroscopic approach in Ref. [103].



collective Hamiltonian [86]. The energy of the collective ground state depends on the softness (both in quadrupole deformation  $\beta_2$  and in triaxial deformation  $\gamma$ ) of the collective energy surface in the vicinity of the ground-state minimum. It differs from approximate values substantially [86]; this could modify calculated  $\tau_{\text{SF}}$  by several orders of magnitude [86,108]. These extremely large theoretical uncertainties in  $\tau_{\text{SF}}$ , coming from the selection of the method (ATDHFB versus GCM+GOA) and the treatment of the ground-state energy, are the reasons why we have not attempted to calculate spontaneous fission half-lives in the present paper.

Fourth, there are some indications that the role of triaxiality can be reduced in dynamical calculations for some nuclei. For example, it was shown in Ref. [104] based on least-action calculations with Skyrme EDF SkM\* that pairing fluctuations act in the direction of restoration of axial symmetry along the fission path in the  $^{240}\text{Pu}$  nucleus. This nucleus is characterized by a relatively modest decrease (approximately 2 MeV) of inner fission barrier height by triaxiality in static calculations. Similar results have also been obtained for  $^{250,264}\text{Fm}$  with similar formalism based on DD-PC1 CEDF in Ref. [106]. The calculations of Refs. [107,108] based on the least-action principle also indicate that the axial symmetry of the fission pathway is restored in many nuclei; they are based on the DFT approach with the Gogny D1S functional [107] and on the macroscopic plus microscopic method [108].

However, not in all nuclei is the effect of triaxiality eliminated by the least-action principle. For example, the least-action fission pathway in  $^{264}\text{Fm}$  is still characterized by triaxiality (although it is somewhat reduced by enhanced pairing as compared with the static fission path) in the calculations based on the Skyrme SkM\* functional [104]. Note that in this nucleus the triaxiality has a large impact (slightly more than 4 MeV) on the height of the inner fission barrier in static calculations. The calculations of Ref. [107] performed with Gogny D1S functionals also indicate that in some nuclei the least-action fission pathway goes through triaxial saddles. More systematic calculations<sup>12</sup> based on the macroscopic plus microscopic method show that the impact of the triaxiality on the least-action fission pathway (and thus on the spontaneous fission half-life) shows up in some nuclei with  $Z = 114$  and becomes much more pronounced in the  $Z \geq 120$  nuclei [108]. Note that the tendency towards restoration of axial symmetry of the fission pathway in the least-action calculations may somewhat be underestimated in Refs. [107,108] because of the neglect of pairing fluctuations.

The analysis of these publications suggests two possible situations in which the least-action fission path will most likely be characterized by triaxiality. In the first one, the decrease of the fission barrier by triaxiality in static calculations is substantial, being on the order of 3–4 MeV [104,108]. In the second one, the ground state is oblate (or possibly soft in the oblate-prolate direction [86]) so that the fission path

across the  $\gamma$  plane is shorter than the one along the  $\gamma = 0^\circ$  line [108]. As discussed in Sec. III and Appendix B only a limited number of nuclei satisfy such conditions. Thus, the restriction to axial symmetry should be considered as a reasonable first approximation. However, one should keep in mind that the values obtained for fission barriers represent upper limits since their possible lowering due to triaxiality is neglected.

## APPENDIX B: POSSIBLE IMPACT OF TRIAXIALITY ON INNER FISSION BARRIERS

The restriction to axial symmetry is one of the approximations used in the present paper which is a consequence of the global character of the study (see detailed discussion presented in the end of Sec. II and in Appendix A). In order to better understand for which nuclei this approximation may be violated (even in least-action calculations with pairing fluctuations included such as those presented in Refs. [104,106]) we consider the examples of potential-energy surfaces obtained in triaxial RHB calculations with the DD-PC1 functional. These PESs calculated for the Sg ( $Z = 106$ ), Ds ( $Z = 110$ ), Fl ( $Z = 114$ ), and Og ( $Z = 118$ ) isotopes with neutron numbers  $N = 192, 202, 212$ , and  $222$  are presented in Fig. 18. They represent the extension of the calculations, executed in a more limited deformation space, the results of which are discussed in Sec. XI of Ref. [66]. The summary of the heights  $E_{\text{triax}}^B$  of triaxial inner fission barriers and the decreases of the fission barrier heights due to triaxiality  $\Delta E^{\text{gain}}$  are presented in Fig. 21 and Table II of Ref. [66]. Note that these superheavy nuclei are selected in such a way that they cover the part of the nuclear chart characterized by both oblate and prolate ground states [see Fig. 5(a)].

The review of existing literature presented in Appendix A suggests two possible scenarios in which the least-action fission path will most likely be characterized by triaxiality. In the first one, the decrease of the fission barrier by triaxiality in static calculations is substantial, being on the order of 3–4 MeV [104,108]. Such decreases are observed in  $^{328}\text{Sg}$  ( $\Delta E^{\text{gain}} = 4.04$  MeV),  $^{310}\text{Og}$  ( $\Delta E^{\text{gain}} = 3.42$  MeV), and  $^{320}\text{Og}$  ( $\Delta E^{\text{gain}} = 4.93$  MeV) [see Figs. 18(d), 18(m), and 18(n) and Table II in Ref. [66]]. In the second scenario, the ground state is oblate (or possibly soft in the oblate-prolate direction [86]) so that the fission path across the  $\gamma$  plane is shorter than the one along the  $\gamma = 0^\circ$  line [108]. This condition is satisfied only in the  $^{306}\text{Fl}$  [see Fig. 18(i)] and  $^{310,320}\text{Og}$  [see Figs. 18(m) and 18(n)] nuclei. Based on general features discussed in Refs. [104,106], the analysis of PESs of remaining nuclei [see Figs. 18(a)–18(c), 18(e)–18(h), 18(j)–18(l), 18(o), and 18(p)] suggests that the least-action fission pathway will be axial in these nuclei when pairing fluctuations are taken into account.

Whether one or another scenario takes place depends on the underlying shell structure (both at the ground state and saddle) defining the topology of potential-energy surfaces in the  $(\beta_2, \gamma)$  plane. Figure 18 shows that the  $N = 192$  isotones are extremely soft in the  $\gamma$  plane with clear tendency for the formation of the near-oblate triaxial ground-state minimum in the Fl and Og nuclei. However, static fission paths from

<sup>12</sup>These calculations are simplified as compared with quoted DFT calculations since they use the fixed single-particle spectrum for all nuclei and neglect the deformations of higher order such as  $\beta_6$  and  $\beta_8$ .

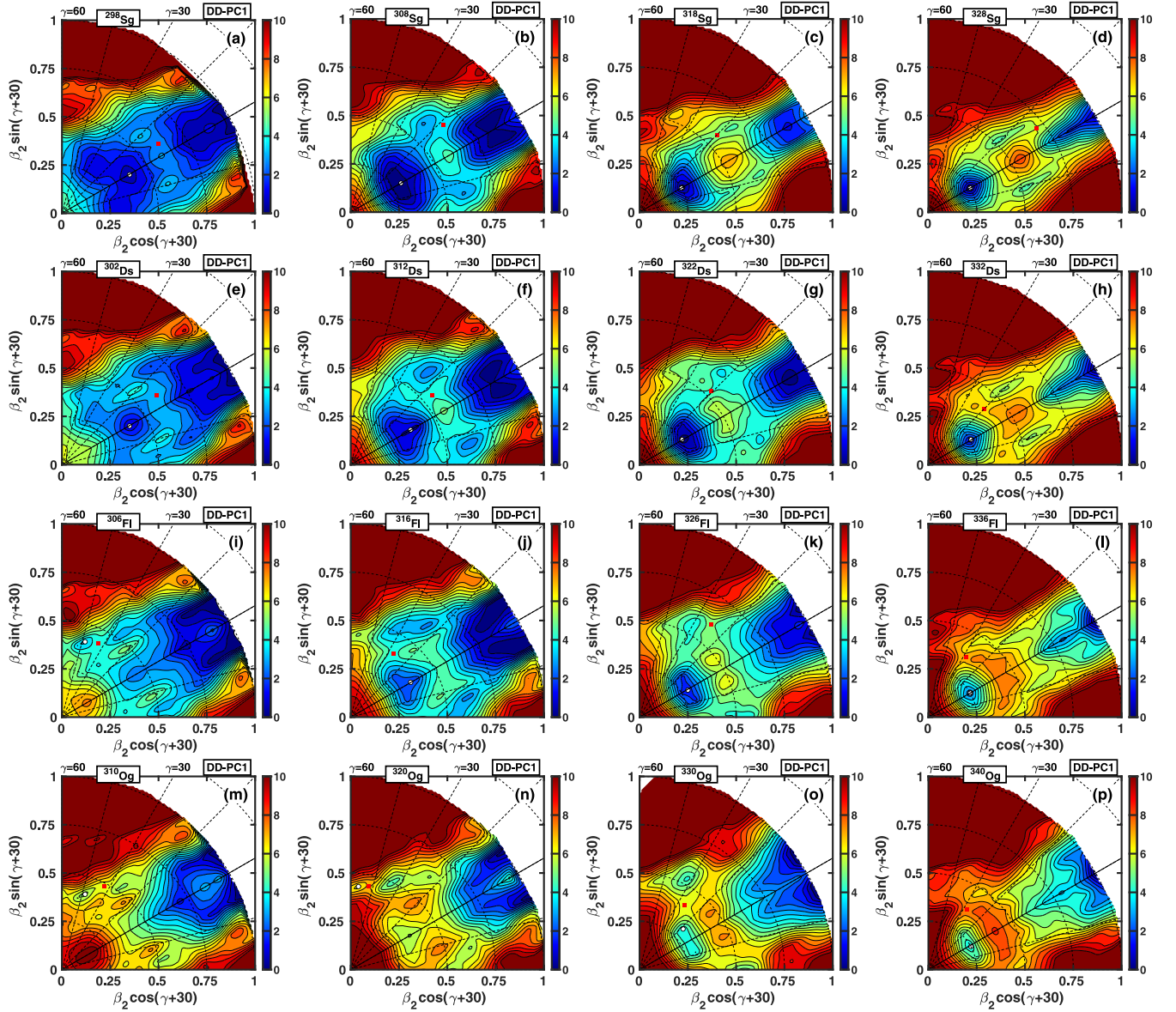


FIG. 18. Potential-energy surfaces of the Sg ( $Z = 106$ ), Ds ( $Z = 110$ ), Fl ( $Z = 114$ ), and Og ( $Z = 118$ ) isotopes with neutron numbers  $N = 192, 202, 212$ , and  $222$  obtained in the triaxial RHB calculations with the DD-PC1 functional. Neutron number is increasing on going from left to right. The energy difference between two neighboring equipotential lines is equal to  $0.5$  MeV. The ground-state minima and saddle points are shown by white circles and red solid squares, respectively.

these minima are characterized by low fission barriers so these nuclei are expected to be unstable. A similar (but slightly less pronounced) situation is also seen for the  $N = 202$  isotones.

The increase of neutron number to  $N = 212$  and  $222$  leads to a better localization of the ground-state minimum at prolate shape and to an increase of fission barrier heights.

- 
- [1] G. Martínez-Pinedo, *Eur. Phys. J.: Spec. Top.* **156**, 123 (2008).  
 [2] V. Liccardo, M. Malheiro, M. S. Hussein, B. V. Carlson, and T. Frederico, *Eur. Phys. J.* **A54**, 221 (2018).  
 [3] D. Kasen, B. Metzger, J. Barnes, E. Quataert, and E. Ramirez-Ruiz, *Nature (London)* **551**, 80 (2017).  
 [4] J. J. Cowan, C. Sneden, J. E. Lawler, A. Aprahamian, M. Wiescher, K. Langanke, G. Martínez-Pinedo, and F.-K. Thielemann, [arXiv:1901.01411v1](https://arxiv.org/abs/1901.01411).  
 [5] F. K. Thielemann, M. Eichler, I. V. Panov, and B. Wehmeyer, *Annu. Rev. Nucl. Part. Sci.* **67**, 253 (2017).  
 [6] B. P. Abbott *et al.*, *Phys. Rev. Lett.* **119**, 161101 (2017).  
 [7] B. P. Abbott *et al.*, *Astrophys. J. Lett.* **848**, L12 (2017).  
 [8] O. Just, A. Bauswein, R. A. Pulpillo, S. Goriely, and H.-T. Janka, *Mon. Not. R. Astron. Soc.* **448**, 541 (2015).  
 [9] Y. Sekiguchi, K. Kiuchi, K. Kyutoku, and M. Shibata, *Phys. Rev. D* **91**, 064059 (2015).

- [10] J. d. J. Mendoza-Temis, M.-R. Wu, K. Langanke, G. Martínez-Pinedo, A. Bauswein, and H.-T. Janka, *Phys. Rev. C* **92**, 055805 (2015).
- [11] G. Martínez-Pinedo, D. Moclaj, N. Zinner, A. Kelić, K. Langanke, I. Panov, B. Pfeiffer, T. Rauscher, K.-H. Schmidt, and F.-K. Thielemann, *Prog. Part. Nucl. Phys.* **59**, 199 (2007).
- [12] S. Goriely, *Eur. Phys. J A* **51**, 22 (2015).
- [13] S. Goriely, J.-L. Sida, J.-F. Lemaître, S. Panebianco, N. Dubray, S. Hilaire, A. Bauswein, and H.-T. Janka, *Phys. Rev. Lett.* **111**, 242502 (2013).
- [14] M. Eichler, A. Arcones, A. Kelić, O. Korobkin, K. Langanke, T. Marketin, G. Martínez-Pinedo, I. Panov, T. Rauscher, S. Rosswog, C. Winteler, N. T. Zinner, and F.-K. Thielemann, *Astrophys. J.* **808**, 30 (2015).
- [15] I. Petermann, K. Langanke, G. Martínez-Pinedo, I. Panov, P.-G. Reinhard, and F.-K. Thielemann, *Eur. Phys. J. A* **48**, 122 (2012).
- [16] S. A. Giuliani, G. Martínez-Pinedo, L. M. Robledo, and M.-R. Wu, *Acta Phys. Pol. B* **48**, 299 (2017).
- [17] S. Goriely and M. Arnould, *Astron. Astrophys.* **312**, 327 (1996).
- [18] S. A. Giuliani, G. Martínez-Pinedo, and L. M. Robledo, *Phys. Rev. C* **97**, 034323 (2018).
- [19] A. Mamdouh, J. Pearson, M. Rayet, and F. Tondeur, *Nucl. Phys. A* **644**, 389 (1998).
- [20] S. Goriely, M. Samyn, and J. M. Pearson, *Phys. Rev. C* **75**, 064312 (2007).
- [21] J. Erler, K. Langanke, H. P. Loens, G. Martínez-Pinedo, and P.-G. Reinhard, *Phys. Rev. C* **85**, 025802 (2012).
- [22] P.-G. Reinhard, *Eur. Phys. J.* **312**, 13 (2018).
- [23] R. Rodríguez-Guzman, Y. M. Humadi, and L. M. Robledo, *Eur. Phys. J. A* **56**, 43 (2020).
- [24] D. Vretenar, A. V. Afanasjev, G. A. Lalazissis, and P. Ring, *Phys. Rep.* **409**, 101 (2005).
- [25] *Extended Density Functionals in Nuclear Structure Physics*, Lecture Notes in Physics Vol. 641, edited by G. A. Lalazissis, P. Ring, and D. Vretenar (Springer-Verlag, Heidelberg, 2004).
- [26] M. Bender, K. Rutz, P.-G. Reinhard, J. A. Maruhn, and W. Greiner, *Phys. Rev. C* **60**, 034304 (1999).
- [27] E. V. Litvinova and A. V. Afanasjev, *Phys. Rev. C* **84**, 014305 (2011).
- [28] W. Koepf and P. Ring, *Nucl. Phys. A* **493**, 61 (1989).
- [29] A. V. Afanasjev and H. Abusara, *Phys. Rev. C* **81**, 014309 (2010).
- [30] U. Hofmann and P. Ring, *Phys. Lett. B* **214**, 307 (1988).
- [31] A. V. Afanasjev and P. Ring, *Phys. Rev. C* **62**, 031302(R) (2000).
- [32] A. V. Afanasjev and H. Abusara, *Phys. Rev. C* **82**, 034329 (2010).
- [33] J. Dobaczewski and J. Dudek, *Phys. Rev. C* **52**, 1827 (1995).
- [34] N. Schunck, J. Dobaczewski, J. McDonnell, J. Moré, W. Nazarewicz, J. Sarich, and M. V. Stoitsov, *Phys. Rev. C* **81**, 024316 (2010).
- [35] N. Hinohara, Z. P. Li, T. Nakatsukasa, T. Nikšić, and D. Vretenar, *Phys. Rev. C* **85**, 024323 (2012).
- [36] S. A. Giuliani and L. M. Robledo, *Phys. Lett. B* **787**, 134 (2018).
- [37] P. G. Reinhard and W. Nazarewicz, *Phys. Rev. C* **81**, 051303(R) (2010).
- [38] J. Dobaczewski, W. Nazarewicz, and P.-G. Reinhard, *J. Phys. G* **41**, 074001 (2014).
- [39] S. E. Agbemava, A. V. Afanasjev, D. Ray, and P. Ring, *Phys. Rev. C* **89**, 054320 (2014).
- [40] M. Bender, P.-H. Heenen, and P.-G. Reinhard, *Rev. Mod. Phys.* **75**, 121 (2003).
- [41] J. Boguta and R. Bodmer, *Nucl. Phys. A* **292**, 413 (1977).
- [42] G. A. Lalazissis, T. Nikšić, D. Vretenar, and P. Ring, *Phys. Rev. C* **71**, 024312 (2005).
- [43] G. A. Lalazissis, S. Karatzikos, R. Fossion, D. P. Arteaga, A. V. Afanasjev, and P. Ring, *Phys. Lett. B* **671**, 36 (2009).
- [44] T. Nikšić, D. Vretenar, and P. Ring, *Phys. Rev. C* **78**, 034318 (2008).
- [45] S. Typel and H. H. Wolter, *Nucl. Phys. A* **656**, 331 (1999).
- [46] S. E. Agbemava, A. V. Afanasjev, and A. Taninah, *Phys. Rev. C* **99**, 014318 (2019).
- [47] S. E. Agbemava, A. V. Afanasjev, D. Ray, and P. Ring, *Phys. Rev. C* **95**, 054324 (2017).
- [48] S. E. Agbemava, A. V. Afanasjev, and P. Ring, *Phys. Rev. C* **93**, 044304 (2016).
- [49] A. V. Afanasjev and S. E. Agbemava, *Phys. Rev. C* **93**, 054310 (2016).
- [50] P. W. Zhao, Z. P. Li, J. M. Yao, and J. Meng, *Phys. Rev. C* **82**, 054319 (2010).
- [51] M. Dutra, O. Lourenco, S. S. Avancini, B. V. Carlson, A. Delfino, D. P. Menezes, C. Providencia, S. Typel, and J. R. Stone, *Phys. Rev. C* **90**, 055203 (2014).
- [52] P.-G. Reinhard, M. Rufa, J. Maruhn, W. Greiner, and J. Friedrich, *Z. Phys. A* **323**, 13 (1986).
- [53] R. Furnstahl, B. D. Serot, and H.-B. Tang, *Nucl. Phys. A* **615**, 441 (1997).
- [54] X. Roca-Maza, X. Viñas, M. Centelles, P. Ring, and P. Schuck, *Phys. Rev. C* **84**, 054309 (2011).
- [55] T. Nikšić, M. Imbrišak, and D. Vretenar, *Phys. Rev. C* **95**, 054304 (2017).
- [56] B. Kumar, S. Singh, B. Agrawal, and S. Patra, *Nucl. Phys. A* **966**, 197 (2017).
- [57] E. Yüksel, T. Marketin, and N. Paar, *Phys. Rev. C* **99**, 034318 (2019).
- [58] A. Taninah, S. E. Agbemava, A. V. Afanasjev, and P. Ring, *Phys. Lett. B* **800**, 135065 (2020).
- [59] S. E. Agbemava, A. V. Afanasjev, T. Nakatsukasa, and P. Ring, *Phys. Rev. C* **92**, 054310 (2015).
- [60] K. Q. Lu, Z. X. Li, Z. P. Li, J. M. Yao, and J. Meng, *Phys. Rev. C* **91**, 027304 (2015).
- [61] S. E. Agbemava and A. V. Afanasjev, *Phys. Rev. C* **96**, 024301 (2017).
- [62] H. Abusara, A. V. Afanasjev, and P. Ring, *Phys. Rev. C* **82**, 044303 (2010).
- [63] V. Prassa, T. Nikšić, G. A. Lalazissis, and D. Vretenar, *Phys. Rev. C* **86**, 024317 (2012).
- [64] B.-N. Lu, J. Zhao, E.-G. Zhao, and S.-G. Zhou, *Phys. Rev. C* **89**, 014323 (2014).
- [65] A. V. Afanasjev, S. E. Agbemava, and A. Gyawali, *Phys. Lett. B* **782**, 533 (2018).
- [66] S. E. Agbemava, A. V. Afanasjev, A. Taninah, and A. Gyawali, *Phys. Rev. C* **99**, 034316 (2019).
- [67] A. V. Afanasjev, S. E. Agbemava, and A. Taninah, *Acta Phys. Pol. B* **13**, 347 (2020).
- [68] Q. S. Zhang, Z. M. Niu, Z. P. Li, J. M. Yao, and J. Meng, *Front. Phys.* **9**, 529 (2014).



- [69] B.-N. Lu, E.-G. Zhao, and S.-G. Zhou, *Phys. Rev. C* **85**, 011301(R) (2012).
- [70] A. V. Afanasjev, P. Ring, and J. König, *Nucl. Phys. A* **676**, 196 (2000).
- [71] H. Kucharek and P. Ring, *Z. Phys. A* **339**, 23 (1991).
- [72] P. Ring, *Prog. Part. Nucl. Phys.* **37**, 193 (1996).
- [73] S. Karatzikos, A. V. Afanasjev, G. A. Lalazissis, and P. Ring, *Phys. Lett. B* **689**, 72 (2010).
- [74] Y. Tian, Z. Y. Ma, and P. Ring, *Phys. Lett. B* **676**, 44 (2009).
- [75] J. F. Berger, M. Girod, and D. Gogny, *Comput. Phys. Commun.* **63**, 365 (1991).
- [76] A. V. Afanasjev and O. Abdurazakov, *Phys. Rev. C* **88**, 014320 (2013).
- [77] J. Dobaczewski, A. V. Afanasjev, M. Bender, L. M. Robledo, and Y. Shi, *Nucl. Phys. A* **944**, 388 (2015).
- [78] H. Abusara, A. V. Afanasjev, and P. Ring, *Phys. Rev. C* **85**, 024314 (2012).
- [79] P. Ring and P. Schuck, *The Nuclear Many-Body Problem* (Springer-Verlag, Berlin, 1980).
- [80] P. Bonche, H. Flocard, and P. H. Heenen, *Comput. Phys. Commun.* **171**, 49 (2005).
- [81] T. Bürvenich, M. Bender, J. A. Maruhn, and P.-G. Reinhard, *Phys. Rev. C* **69**, 014307 (2004).
- [82] A. Staszczak, A. Baran, J. Dobaczewski, and W. Nazarewicz, *Phys. Rev. C* **80**, 014309 (2009).
- [83] P. Möller, A. J. Sierk, T. Ichikawa, A. Iwamoto, R. Bengtsson, H. Uhrenholt, and S. Åberg, *Phys. Rev. C* **79**, 064304 (2009).
- [84] W. D. Myers and W. J. Świątecki, *Phys. Rev. C* **60**, 014606 (1999).
- [85] M. Arnould and S. Goriely, *Prog. Part. Nucl. Phys.* **112**, 103766 (2020).
- [86] Z. Shi, A. V. Afanasjev, Z. P. Li, and J. Meng, *Phys. Rev. C* **99**, 064316 (2019).
- [87] T. Sil, S. K. Patra, B. K. Sharma, M. Centelles, and X. Viñas, *Phys. Rev. C* **69**, 044315 (2004).
- [88] M. Bender, W. Nazarewicz, and P.-G. Reinhard, *Phys. Lett. B* **515**, 42 (2001).
- [89] W. Zhang, J. Meng, S. Zhang, L. Geng, and H. Toki, *Nucl. Phys. A* **753**, 106 (2005).
- [90] A. V. Afanasjev, S. E. Agbemava, D. Ray, and P. Ring, *Phys. Rev. C* **91**, 014324 (2015).
- [91] Evaluated Nuclear Structure Data File (ENSDF), Brookhaven National Laboratory, <http://www.nndc.bnl.gov/ensdf/>. ENSDF is based on the publications presented in Nuclear Data Sheets, which is a standard for evaluated nuclear data. Accessed 2015.
- [92] X. Xia, Y. Lim, P. Zhao, H. Liang, X. Qu, Y. Chen, H. Liu, L. Zhang, S. Zhang, Y. Kim, and J. Meng, *At. Data Nucl. Data Tables* **121-122**, 1 (2018).
- [93] A. V. Afanasjev, S. E. Agbemava, D. Ray, and P. Ring, *Phys. Lett. B* **726**, 680 (2013).
- [94] M. Wang, G. Audi, A. H. Wapstra, F. G. Kondev, M. MacCormick, X. Xu, and B. Pfeiffer, *Chin. Phys. C* **36**, 1603 (2012).
- [95] J. V. E. Viola and G. T. Seaborg, *J. Inorg. Nucl. Chem.* **28**, 741 (1966).
- [96] A. Sobczewski, Z. Patyk, and S. Cwiok, *Phys. Lett. B* **224**, 1 (1989).
- [97] T. Dong and Z. Ren, *Eur. Phys. J. A* **26**, 69 (2005).
- [98] A. Budaca, R. Budaca, and I. Silisteanu, *Nucl. Phys. A* **951**, 60 (2016).
- [99] G. Royer, *J. Phys. G* **26**, 1149 (2000).
- [100] C. Y. Wong, *Ann. Phys. (NY)* **77**, 279 (1973).
- [101] Y. T. Oganessian and S. N. Dmitriev, *Rus. Chem. Rev.* **85**, 901 (2016).
- [102] S. Cwiok, P.-H. Heenen, and W. Nazarewicz, *Nature (London)* **433**, 705 (2005).
- [103] A. Dobrowolski, K. Pomorski, and J. Bartel, *Phys. Rev. C* **75**, 024613 (2007).
- [104] J. Sadhukhan, J. Dobaczewski, W. Nazarewicz, J. A. Sheikh, and A. Baran, *Phys. Rev. C* **90**, 061304(R) (2014).
- [105] K. Benrabia, D. E. Medjadi, M. Imadalou, and P. Quentin, *Phys. Rev. C* **96**, 034320 (2017).
- [106] J. Zhao, B.-N. Lu, T. Nikšić, D. Vretenar, and S.-G. Zhou, *Phys. Rev. C* **93**, 044315 (2016).
- [107] J.-P. Delaroche, M. Girod, H. Goutte, and J. Libert, *Nucl. Phys. A* **771**, 103 (2006).
- [108] R. Gherghescu, J. Skalski, Z. Patyk, and A. Sobczewski, *Nucl. Phys. A* **651**, 237 (1999).
- [109] N. Schunck and L. M. Robledo, *Rep. Prog. Phys.* **79**, 116301 (2016).
- [110] S. A. Giuliani, Z. Matheson, W. Nazarewicz, E. Olsen, P.-G. Reinhard, J. Sadhukhan, B. Schuettrumpf, N. Schunck, and P. Schwerdtfeger, *Rev. Mod. Phys.* **91**, 011001 (2019).
- [111] N. Schindzielorz, J. Erler, P. Klupfel, P. G. Reinhard, and G. Hager, *Int. J. Mod. Phys. E* **18**, 773 (1981).